JCB Journal of Cell Biology

TOOLS

High-fidelity reconstitution of stress granules and nucleoli in mammalian cellular lysate

Brian D. Freibaum[1*], James Messing[1,2*], Peiguo Yang[1], Hong Joo Kim[1], and J. Paul Taylor[1,2]

Liquid–liquid phase separation (LLPS) is a mechanism of intracellular organization that underlies the assembly of a variety of RNP granules. Fundamental biophysical principles governing LLPS during granule assembly have been revealed by simple in vitro systems, but these systems have limitations when studying the biology of complex, multicomponent RNP granules. Visualization of RNP granules in cells has validated key principles revealed by simple in vitro systems, but this approach presents difficulties for interrogating biophysical features of RNP granules and provides limited ability to manipulate protein, nucleic acid, or small molecule concentrations. Here, we introduce a system that builds upon recent insights into the mechanisms underlying RNP granule assembly and permits high-fidelity reconstitution of stress granules and the granular component of nucleoli in mammalian cellular lysate. This system fills the gap between simple in vitro systems and live cells and allows for a variety of studies of membraneless organelles, including the development of therapeutics that modify properties of specific condensates.

Introduction

A wealth of insights over the past decade has revealed the important role of biomolecular condensation in organizing cell biology through spatial and temporal control over cellular components (Banani et al., 2017). RNA metabolism in particular is governed by the formation of large, complex condensates known as RNP granules that contain hundreds of distinct proteins and RNAs (Nedelsky and Taylor, 2019). RNP granules are abundant in the nucleus (e.g., nucleoli, Cajal bodies, and speckles) and in the cytoplasm (e.g., P bodies and stress granules). Each type of RNP granule is defined by a distinct composition of proteins and RNA and contributes in myriad ways to regulation of RNA metabolism. The environment within condensates can contribute to establishing RNA three-dimensional structure, assembling large complexes such as ribosomal subunits, implementing splicing, and promoting chemical modifications. RNP granules can also aid in the long-range transport of mRNAs, regulate their translation, and control their degradation (Frottin et al., 2019; Galganski et al., 2017; Neugebauer, 2017; Tauber et al., 2020; Youn et al., 2019). RNP granules may also provide compartments for a host of non–RNA-related functions (Kedersha et al., 2013; Schisa, 2019).

RNP granules assemble by liquid–liquid phase separation (LLPS), which occurs when proteins and protein-laden RNAs that are dispersed in the cytoplasm or nucleoplasm (soluble phase) coalesce into a concentrated state (condensed phase; Brangwynne et al., 2009). In this condensed phase, the proteins and RNA behave as a single organelle with liquid-like properties, although the individual constituents remain in dynamic equilibrium with the surrounding intracellular milieu. The dynamic behavior of condensates reflects the nature of the interactions that underlie their assembly—namely, weak, transient interactions among multivalent biomolecules that form noncovalent cross-links of varying strengths and durations. At low concentration, the individual proteins and protein-laden RNAs remain in a dispersed state. However, when the system becomes populated with sufficient cross-links to form a system-spanning network, defined as the percolation threshold, LLPS occurs, giving rise to a condensate that is distinct from its cytoplasmic or nuclear milieu (Harmon et al., 2017). Membraneless organelles provide a strategic advantage over membrane-bound organelles because they not only concentrate macromolecules in space but can also assemble and disassemble rapidly and permit rapid exchange of constituents with the surrounding cytoplasm or nucleoplasm. The material properties of condensates, including viscosity, elasticity, and surface tension, are directly linked to condensate function, and alterations to material properties in RNP granules, and stress granules in particular, have been linked to neurodegenerative diseases such as amyotrophic lateral sclerosis (ALS) and frontotemporal dementia (Nedelsky and Taylor, 2019).

[1]Department of Cell and Molecular Biology, St. Jude Children's Research Hospital, Memphis, TN; [2]Howard Hughes Medical Institute, Chevy Chase, MD.

*B.D. Freibaum and J. Messing contributed equally to this paper; Correspondence to J. Paul Taylor: jpaul.taylor@stjude.org.

© 2021 Freibaum et al. This article is distributed under the terms of an Attribution–Noncommercial–Share Alike–No Mirror Sites license for the first six months after the publication date (see http://www.rupress.org/terms/). After six months it is available under a Creative Commons License (Attribution–Noncommercial–Share Alike 4.0 International license, as described at https://creativecommons.org/licenses/by-nc-sa/4.0/).

Recent studies have yielded insight into the logic that defines the percolation threshold for complex condensates. For stress granules, this threshold is encoded by the network of protein–protein, protein–RNA, and RNA–RNA interactions that drives LLPS (Guillén-Boixet et al., 2020; Sanders et al., 2020; Yang et al., 2020). Each component of this network contributes toward the sum of interactions required to reach the percolation threshold. Importantly, however, some components contribute more than others; specifically, the contribution of individual nodes correlates with their centrality within the network. For example, in stress granules there are ∼36 proteins that, together with RNA, provide the majority of the cross-links that set the percolation threshold beyond which LLPS occurs (Yang et al., 2020). Among these proteins, the most central node for the stress granule network is G3BP1, which undergoes LLPS with RNA to initiate granule assembly (Guillén-Boixet et al., 2020; Sanders et al., 2020; Yang et al., 2020). The centrality of G3BP1 in stress granule assembly has also been shown in an optogenetic system in which light-induced LLPS of G3BP1 was sufficient to drive the formation of stress granules in cells even in the absence of exogenous stress (Zhang et al., 2019). In contrast, light-induced LLPS of other stress granule proteins, including TIA1, FUS, and TDP-43, led to the formation of liquid-like droplets that had neither the biophysical properties nor the components of stress granules induced by cellular stress (Zhang et al., 2019). Correspondingly, stress granule assembly can also be triggered by raising the local concentration of free mRNA within the core protein–RNA interaction network (Van Treeck et al., 2018). This was nicely demonstrated in a recent study using yeast lysates, in which the addition of specific mRNAs was sufficient to trigger the formation of structures that closely resembled stress granules formed in intact cells (Begovich and Wilhelm, 2020).

Fundamental principles governing the assembly of RNP granules have emerged from the study of simple, reconstituted systems of one or several molecules (Berry et al., 2015; Mitrea et al., 2018; Molliex et al., 2015). However, this approach has been inadequate for studying the formation of complex, dynamic, multicomponent condensates such as RNP granules. Likewise, visualization of RNP granules in cells has validated many of the principles revealed by in vitro systems, but these approaches are confounded by challenges with interrogating many key features of RNP granules, most notably their material properties, which are intimately related to granule function (Elbaum-Garfinkle, 2019). Additionally, the biochemical purification of stress granule cores from stressed cells has provided valuable insight into the RNA and protein components found within the stress granule core (Jain et al., 2016; Khong et al., 2017). Nevertheless, such in vivo systems suffer from limited ability to rapidly and precisely manipulate protein, nucleic acid, and small molecule concentrations. Cell-based systems also present challenges for early-stage drug development programs because intact cells are impermeable to many small molecules and those that do permeate cells often lead to cytotoxicity.

Here, we have taken advantage of recent insights into the mechanisms underlying RNP granule assembly to bridge the gap between highly simplistic reconstitution and intact cells. Specifically, we use insight into the network topology underlying the assembly of RNP granules to guide the methodology for their in vitro reconstitution from whole cell lysate (Yang et al., 2020). Thus, our manuscript describes a protein-based system in which a mammalian cellular lysate is seeded with a purified protein (i.e., G3BP1 or NPM1) to recapitulate the formation of a distinct RNP granule in a cellular lysate. Thorough analysis reveals that lysate granules induced by G3BP1 are highly similar to stress granules in their dynamic liquid properties as well as their RNA and protein composition, whereas lysate granules induced by NPM1 recapitulate the RNA and protein composition of the granular compartment of nucleoli.

Results

Seeding of purified G3BP1 in a cell lysate induces LLPS

To establish an in vitro lysate system in which LLPS and stress granule formation could be recapitulated, deeply interrogated, and experimentally manipulated, we generated a cellular extract from U2OS cells stably expressing G3BP1-GFP (Yang et al., 2020). Cells were collected by centrifugation, lysed briefly in minimal lysis buffer, and centrifuged to remove cellular debris, and the supernatant was retained to create an extract consisting of both cytoplasmic and nuclear components that we hereafter refer to as the cellular lysate (Fig. 1 A and Fig. S1 A; and Materials and methods). No liquid condensates or inhomogeneities were detected in these lysates by differential interference contrast (DIC) and fluorescent imaging (Fig. 1 B). Beginning with a baseline G3BP1 concentration of ∼250 nM in cells (150 nM G3BP1-GFP and 100 nM endogenous G3BP1; Fig. S1 B) and following dilution by ∼11-fold in lysis buffer (resulting in ∼23 nM G3BP1 in lysate), we added increasing concentrations of recombinant, purified G3BP1 or other proteins to this lysate while monitoring the lysate by DIC and fluorescent microscopy (Fig. 1 A). Dense, spherical, liquid granules containing G3BP1-GFP were induced when the total concentration of G3BP1 was increased by 2.5–5 μM with purified protein (Fig. 1 B), consistent with the threshold effect that characterizes LLPS. Taking into consideration the baseline concentration of ∼250 nM G3BP1 in the cells, this critical seeding threshold corresponded to an ∼10-fold increase in cellular G3BP1 concentration. Introducing increasing amounts of the G3BP1 protein to the lysate resulted in increased condensation (Fig. 1 B). In the absence of lysate, purified G3BP1 alone did not form condensates with concentrations up to 100 μM (Fig. 1 B and data not shown), consistent with our previous findings (Yang et al., 2020) and indicating that components within the cell lysate are required for robust LLPS of G3BP1. In contrast to G3BP1, the addition of increasing concentrations of BSA or hnRNPA1 (a protein that readily undergoes LLPS) did not induce granule formation or other condensation, indicating specificity in the formation of condensates within cell lysates (Fig. 1 C). The ability of G3BP1 to initiate condensation in lysate, whereas some other proteins do not, is consistent with the high-ranking centrality of G3BP1 in the network of stress granule constituents (Yang et al., 2020).

We recently showed that both the dimerization domain (NTF2L) and the RNA-binding domain of G3BP1 are required for

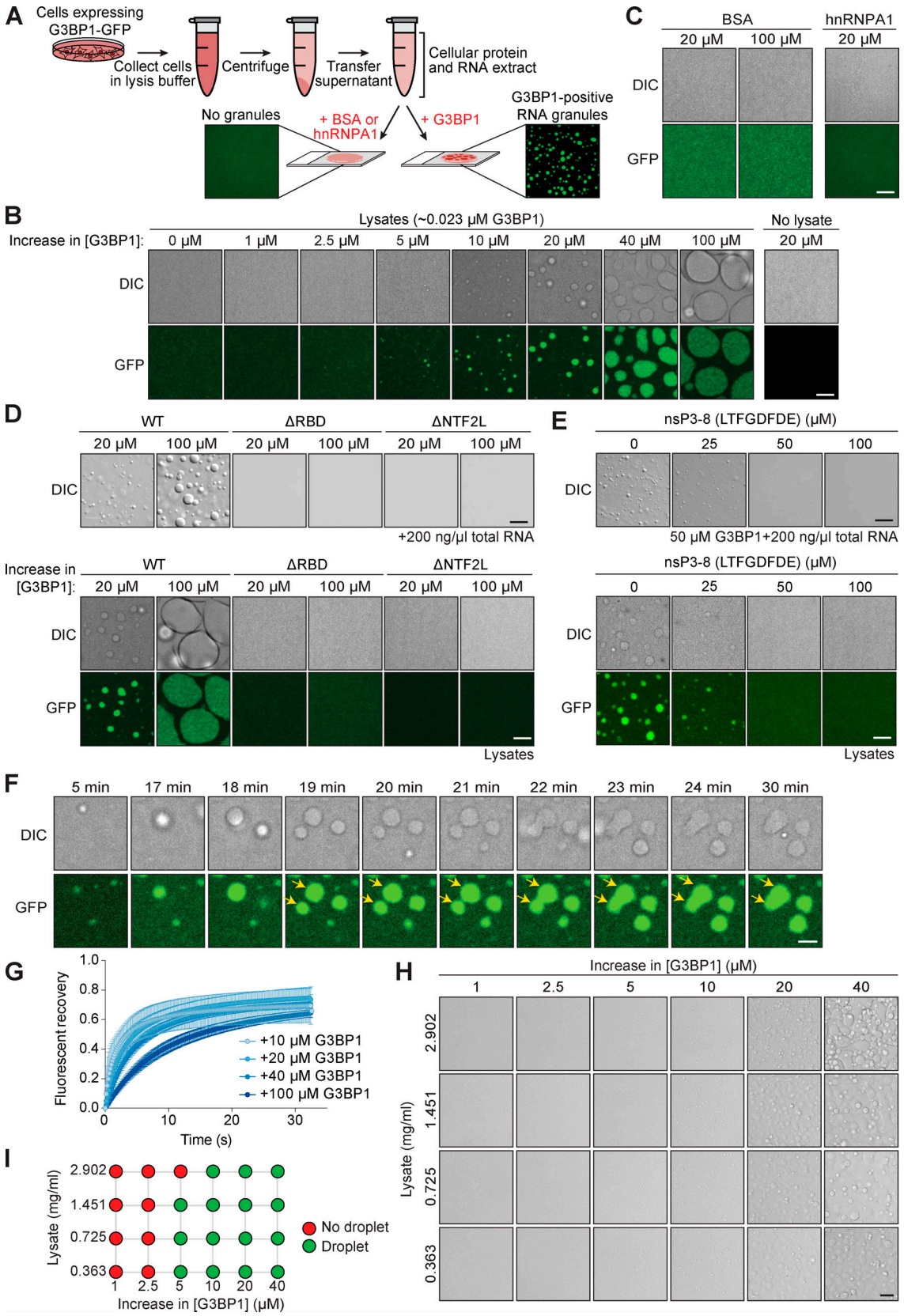

Figure 1. **Addition of purified G3BP1 protein to a cell lysate induces LLPS to assemble G3BP1-positive granules. (A)** Schematic illustrating the generation of lysate granules from U2OS cells stably expressing G3BP1-GFP. **(B)** Addition of G3BP1 purified protein to a cell lysate from G3BP1-GFP U2OS cells induces LLPS of G3BP1 in a dose-dependent manner when the concentration of G3BP1 is increased by 5 μM with purified protein. LLPS is strongly inhibited in the absence of lysate. Images were taken 30 min following formation of lysate granules. Scale bar, 10 μm. **(C)** Addition of BSA or hnRNPA1 does not induce

LLPS in lysates from G3BP1-GFP U2OS cells. Scale bar, 10 µm. **(D)** Purified G3BP1 lacking the RNA-binding domain (ΔRBD) or dimerization domain (ΔNTF2L) is unable to induce LLPS with RNA (top), nor does it induce LLPS in U2OS cell lysates expressing G3BP1-GFP (bottom). Scale bar, 10 µm. **(E)** Both two-component LLPS of G3BP1 and RNA (top) as well as LLPS induced by increasing the concentration of G3BP1 by 20 µM in U2OS cell lysates expressing G3BP1-GFP (bottom) are inhibited by the nsP3 peptide (LTFGDFDE, nsP3-8 hereafter) from Chikungunya virus. Scale bar, 10 µm. **(F)** Liquid properties of G3BP1-positive granules induced by increasing the concentration of G3BP1 by 20 µM using purified G3BP1 in U2OS cell lysates expressing G3BP1-GFP. Granules grow and fuse over time. Arrows indicate a fusion event between granules. Scale bar, 5 µm. **(G)** FRAP performed on G3BP1-GFP within lysate granules induced by increasing concentrations of purified G3BP1 show that granules are mobile. Graph represents mean ± SD, n = 10 granules per condition. **(H and I)** Brightfield phase diagram (H) with varying G3BP1 and lysate concentrations 60 min after induction (scale bar, 20 µm) and pictogram (I) indicating whether droplet formation was observed for indicated increases in G3BP1 concentration and lysate concentrations.

RNA-dependent LLPS in a simple in vitro reconstitution system and also for stress granule assembly in cells (Yang et al., 2020). Consistent with these observations, G3BP1 mutants lacking these domains failed to induce LLPS of G3BP1 with RNA in vitro, as well as within our lysate system (Fig. 1 D), demonstrating that these G3BP1 granules have the same domain requirements for LLPS as those observed in other systems.

We next examined the effect of nonstructural protein 3 (nsP3), a nonstructural protein derived from the Chikungunya virus that potently inhibits LLPS of G3BP1 by interacting with the NTF2L domain (Fros et al., 2012). LLPS of G3BP1 with RNA as well as granule formation within our lysate system were both inhibited in a dose-dependent manner by the addition of an eight–amino acid peptide representing the Phe-Gly-Asp-Phe (FGDF) motif from nsP3 (Fig. 1 E; Panas et al., 2014). These results demonstrate that G3BP1-induced lysate granules reflect a G3BP1-dependent condensation that exhibits the same sensitivity to nsP3 peptide as G3BP1 LLPS with RNA in vitro and stress granule assembly in cells.

G3BP1-induced lysate granules exhibited liquid properties similar to those observed in G3BP1 droplets produced in a simple in vitro reconstitution system as well as in stress granules assembled in cells (Yang et al., 2020), including fusion events to create granules that grew in volume over time (Fig. 1 F, Video 1, and Video 2), dynamic exchange of constituents with the light phase as assessed by FRAP (Fig. 1 G and Video 3), and dissolution of the condensates by 1,6-hexanediol, a compound that disrupts weak hydrophobic interactions and thus disrupts LLPS (Ribbeck and Görlich, 2002), either 15 or 30 min following the addition of recombinant G3BP1 (Fig. S1 C). Furthermore, manipulating the relative concentrations of cell lysate and purified G3BP1 enabled the construction of a full phase diagram (Fig. 1, H and I). This diagram revealed a characteristic phase boundary, a fundamental property of LLPS (Fig. 1, H and I).

G3BP1-induced lysate granules and stress granules have similar protein composition

Stress granules are complex condensates that comprise hundreds of distinct proteins and RNAs (Khong et al., 2017; Youn et al., 2019). In cells, stress granule assembly is initiated by a rise in cytoplasmic free mRNA concentration that typically accompanies inhibition of translation initiation. The rise in mRNA concentration is sensed by G3BP1, which functions as a molecular switch to trigger stress granule assembly via RNA-dependent LLPS (Guillén-Boixet et al., 2020; Sanders et al., 2020; Yang et al., 2020). The intracellular concentration of G3BP1 sets the threshold for how high mRNA concentrations must rise to initiate stress granule assembly; indeed, with a sufficiently high concentration of G3BP1, stress granule assembly can be initiated even without a pronounced rise in cytoplasmic mRNAs (Yang et al., 2020). The importance of G3BP1 reflects its centrality within the core network of interactions that underlie stress granule assembly (Yang et al., 2020). We have shown this phenomenon experimentally within cells, wherein enforcing LLPS of G3BP1 using an optogenetic approach is sufficient to trigger the full cascade of stress granule assembly as assessed by protein composition of the resulting granules (Zhang et al., 2019). In contrast, enforcing LLPS of other stress granule proteins, including TIA1, FUS, and TDP-43, produced liquid droplets that did not reconstitute stress granules (Zhang et al., 2019).

We therefore hypothesized that condensation initiated by G3BP1 in cellular lysate might recapitulate full-fledged stress granule assembly. Thus, we sought to characterize the protein composition of G3BP1-induced lysate granules and assess their similarities to intracellular stress granules. We began by interrogating the protein composition of lysate granules using an indirect immunofluorescence approach. To visualize the incorporation of endogenous proteins into lysate granules, we preconjugated primary antibodies with secondary antibody and added these to the lysate granules immediately following induction by increasing the concentration of G3BP1 by 20 µM using purified G3BP1. We used antibodies against six proteins known to be stress granule constituents, five of which have been identified as members of the core stress granule protein–protein interaction network (CAPRIN1, PRRC2C, USP10, UBAP2L, and CSDE1; Yang et al., 2020) and one additional validated stress granule marker, PABPC1 (Kedersha et al., 2000). All six proteins were confirmed to accumulate in lysate granules (Fig. 2 A). In contrast, when we used antibodies against a collection of proteins known to be absent from stress granules (actin, DCP1A, FKBP12, TOM20, and GOLGA3), all were found to be absent from lysate granules (Fig. 2 A).

To further assess lysate granule composition, we used CRISPR-Cas9 in U2OS cells to introduce fluorescent tags into endogenous genes. For example, we created dual-tagged cell U2OS lines in which endogenous G3BP1 and TDP-43 were fused to mRuby3 and GFP, respectively. When lysates were generated from these cells and supplemented with purified G3BP1, these endogenous proteins were robustly recruited to lysate granules (Fig. 2 B). Similarly, we generated cells stably expressing fluorescently tagged ATXN2L and TIA1. These canonical stress granule constituents were also robustly recruited to lysate granules, whereas the GFP tag expressed alone was excluded

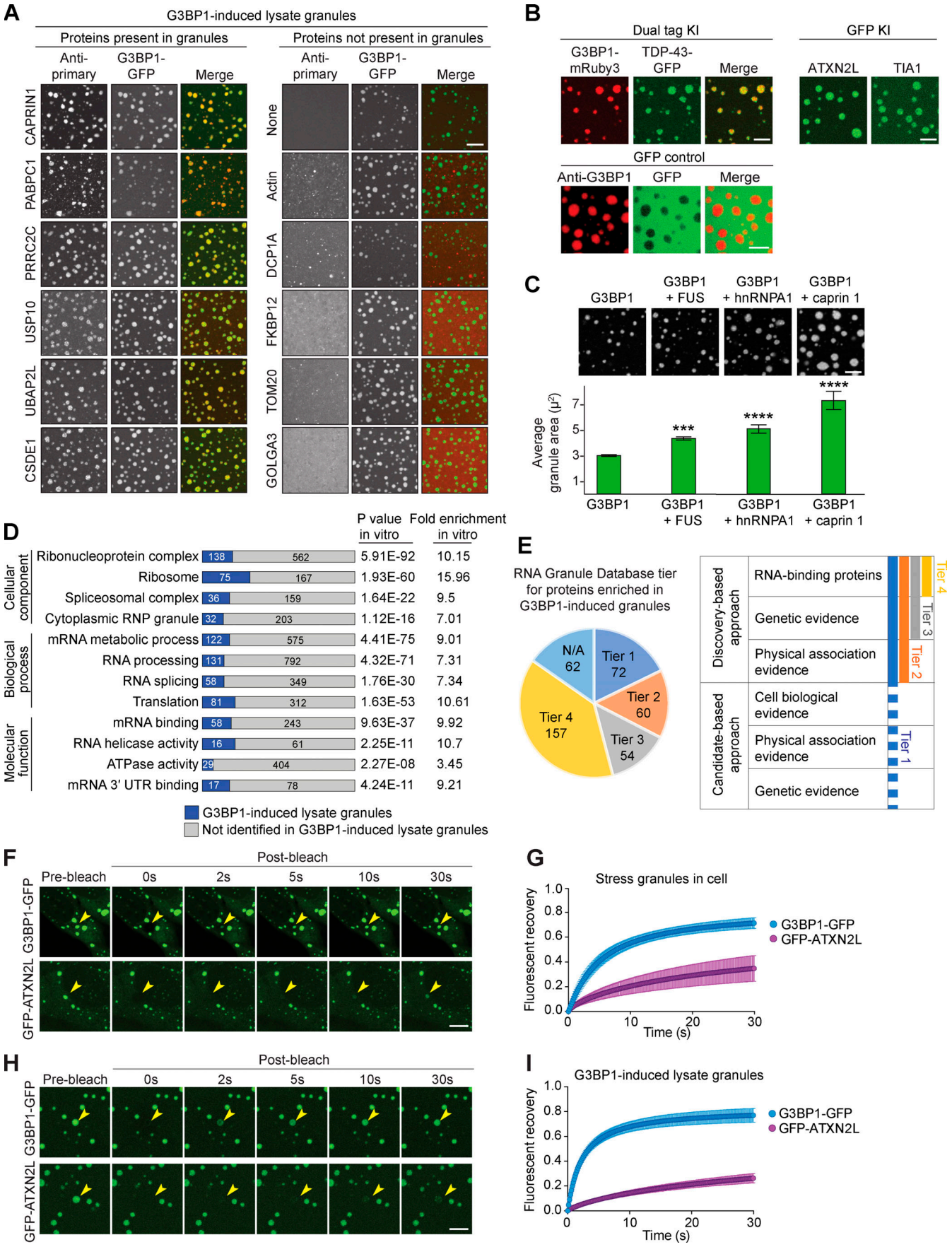
A
G3BP1-induced lysate granules
Proteins present in granules
Proteins not present in granules
Anti-primary
G3BP1-GFP
Merge
CAPRIN1
PABPC1
PRRC2C
USP10
UBAP2L
CSDE1
None
Actin
DCP1A
FKBP12
TOM20
GOLGA3
B
Dual tag KI
G3BP1-mRuby3
TDP-43-GFP
Merge
GFP KI
ATXN2L
TIA1
GFP control
Anti-G3BP1
GFP
Merge
C
G3BP1
G3BP1 + FUS
G3BP1 + hnRNPA1
G3BP1 + caprin 1
Average granule area (μ²)
***
****
****
D
P value in vitro
Fold enrichment in vitro
Cellular component
Biological process
Molecular function
Ribonucleoprotein complex 138 562 5.91E-92 10.15
Ribosome 75 167 1.93E-60 15.96
Spliceosomal complex 36 159 1.64E-22 9.5
Cytoplasmic RNP granule 32 203 1.12E-16 7.01
mRNA metabolic process 122 575 4.41E-75 9.01
RNA processing 131 792 4.32E-71 7.31
RNA splicing 58 349 1.76E-30 7.34
Translation 81 312 1.63E-53 10.61
mRNA binding 58 243 9.63E-37 9.92
RNA helicase activity 16 61 2.25E-11 10.7
ATPase activity 29 404 2.27E-08 3.45
mRNA 3′ UTR binding 17 78 4.24E-11 9.21
G3BP1-induced lysate granules
Not identified in G3BP1-induced lysate granules
E
RNA Granule Database tier for proteins enriched in G3BP1-induced granules
N/A 62
Tier 1 72
Tier 2 60
Tier 3 54
Tier 4 157
Discovery-based approach
Candidate-based approach
RNA-binding proteins
Genetic evidence
Physical association evidence
Cell biological evidence
Physical association evidence
Genetic evidence
Tier 4
Tier 3
Tier 2
Tier 1
F
Pre-bleach
Post-bleach
0s
2s
5s
10s
30s
G3BP1-GFP
GFP-ATXN2L
G
Stress granules in cell
Fluorescent recovery
Time (s)
G3BP1-GFP
GFP-ATXN2L
H
Pre-bleach
Post-bleach
0s
2s
5s
10s
30s
G3BP1-GFP
GFP-ATXN2L
I
G3BP1-induced lysate granules
Fluorescent recovery
Time (s)
G3BP1-GFP
GFP-ATXN2L

Figure 2. **Protein composition of G3BP1-induced lysate granules resembles the protein composition of stress granules in cells. (A)** Primary antibodies conjugated to Alexa Fluor 647 secondary antibody were used to visualize proteins known to be stress granule constituents (left) and proteins known to be absent from stress granules (right). Scale bar, 10 µm. **(B)** Endogenous canonical stress granule constituents (TDP-43, ATXN2L, TIA1) were fluorescently tagged using CRISPR-Cas9 KI in U2OS cells. Endogenous TDP-43, ATXN2L, and TIA1 all localized to lysate granules. GFP from U2OS cells stably expressing GFP did not localize to lysate granules as visualized with anti-G3BP1 staining. Scale bars, 10 µm. **(C)** Overexpression of GFP-tagged stress granule constituents (FUS, hnRNPA1, or caprin 1) by transfection resulted in larger granules, demonstrating positive cooperativity. Lysates were seeded at equal concentrations. Images show granules 2 h after induction by increasing the G3BP1 concentration by 20 µM and associated quantification of average granule size at 2 h. Scale bar, 10 µm. Graph represents mean ± SD, n = 5 independent representative fields. ANOVA with Dunnett's test was used to calculate P values for control versus FUS (***, P = 0.0002), hnRNPA1 (****, P < 0.0001), and caprin 1 (****, P < 0.0001). **(D)** Gene ontology analysis of proteins found to be enriched within G3BP1-induced lysate granules by mass spectrometry reveals that lysate granules share common features with cellular RNP granules. **(E)** Most proteins identified within lysate granules appear within the RNP Granule Database (http://rnagranuledb.lunenfeld.ca/) as Tier 1–4 proteins, indicating that lysate granules share common components with stress granules. **(F–I)** FRAP performed on G3BP1-GFP and GFP-ATXN2L shows similar mobility between stress granules within U2OS cells induced with 0.5 mM $NaAsO_2$ (F and G) and lysate granules induced by increasing G3BP1 concentration by 20 µM using purified G3BP1 (H and I). Arrowheads indicate stress granules or lysate granules on which FRAP was performed. All images were acquired 30 min after induction. Scale bars, 10 µm. Graphs in G and I represent mean ± SD, n = 10 or 11 granules for G3BP1-GFP and GFP-ATXN2L from either cells or lysate.

from lysate granules (Fig. 2 B). We also made use of the observation that overexpression of numerous stress granule constituent proteins is known to promote stress granule assembly (Kedersha et al., 2016). This phenomenon reflects positive cooperativity, which lowers the network-encoded threshold for LLPS (Yang et al., 2020). Consistent with prior observations in cells, we found that lysate generated from cells overexpressing FUS, hnRNPA1, or caprin 1 strongly promoted lysate granule assembly (Fig. 2 C and Fig. S2).

We also performed a comprehensive analysis of proteins recruited to G3BP1-induced lysate granules using mass spectrometry. For these experiments, we used liquid chromatography–tandem mass spectrometry (LC-MS/MS) to analyze sedimented granules induced by increasing the concentration of G3BP1 by 20 µM, using an unseeded lysate as a negative control. We found 405 proteins enriched in G3BP1-induced granules compared with control, including 267 proteins enriched >10-fold relative to control (Table S1). Gene ontology analysis revealed that the lysate granule proteome was highly enriched for proteins known to comprise RNP complexes, stress granules, and other aspects of RNA metabolism (Fig. 2 D). To assess the similarity of this proteome to the proteome of stress granules assembled in cells, we compared the proteins found in lysate granules with the list of stress granule proteins cataloged in the RNA Granule Database, an online catalog of proteins that have been reported in the literature as constituents of stress granules (Youn et al., 2019). Proteins within this curated database are assigned to "quality tiers" based on the extent of evidence and validation identifying each protein as a constituent of stress granules, with Tier 1 proteins representing the most extensively validated proteins. Of the 405 total proteins identified in the lysate granules, 343 were present in the RNA Granule Database (Fig. 2 E). This comparison indicates that the protein composition of G3BP1-induced lysate granules represents a high-fidelity recapitulation of stress granules that arise within cells.

Like other complex biological condensates, stress granules are highly dynamic structures in which constituents exchange between the dense phase and the surrounding cellular milieu with differing mobilities. For example, FRAP analysis demonstrated that both G3BP1 and ATXN2L are mobile within arsenite-induced stress granules, although G3BP1 shows a more rapid recovery and larger mobile fraction than ATXN2L after photobleaching (Fig. 2, F and G; and Video 4). Induction of lysate granules by a 20-µM increase in G3BP1 concentration produced granules similar in size (1–3 µm) to those induced in cells by arsenite treatment, and remarkably, FRAP analysis demonstrated that the relative dynamics of G3BP1 and ATXN2L were preserved in lysate granules (Fig. 2, H and I; and Video 5).

Taken together, these experiments demonstrate that lysate granules are condensates that arise through LLPS triggered by G3BP1 specifically. They follow the molecular rules of G3BP1 LLPS as defined in previous studies and are complex, dynamic condensates that recapitulate the protein composition of stress granules with high fidelity.

G3BP1-induced lysate granules and stress granules have highly similar RNA composition

Stress granules are composed of not only proteins but also mRNAs. The specific enrichment of mRNAs in stress granules is consistent with the binding preference of G3BP1 and other stress granule proteins for mRNA (Yang et al., 2020). While >12,000 individual mRNAs and some noncoding RNAs have been identified in stress granules, the targeting efficiency varies widely, with relative enrichment of some transcripts and relative depletion of others (Khong et al., 2017). mRNA accumulation in stress granules correlates with longer coding and UTR regions as well as poor translatability (Khong et al., 2017). We therefore next investigated the RNA composition of lysate granules to assess their similarity to stress granules assembled in cells. We began by examining the presence of mRNA within lysate granules using a fluorescent oligo-dT probe, which revealed enrichment of polyA-mRNA within granules (Fig. 3 A). Indeed, the RNA component seems essential to lysate granule assembly, since the addition of RNase to the lysate prevented assembly of granules (Fig. 3 A). Within cells, the availability of mRNA for stress granule assembly can be modulated through the use of small molecules such as cycloheximide, which blocks stress granule assembly by inhibiting the runoff of mRNA on ribosomes and preventing the local accumulation of free mRNA (Lui et al., 2014; Mollet et al., 2008). This inhibition of stress granule assembly can be recapitulated in the lysate granules

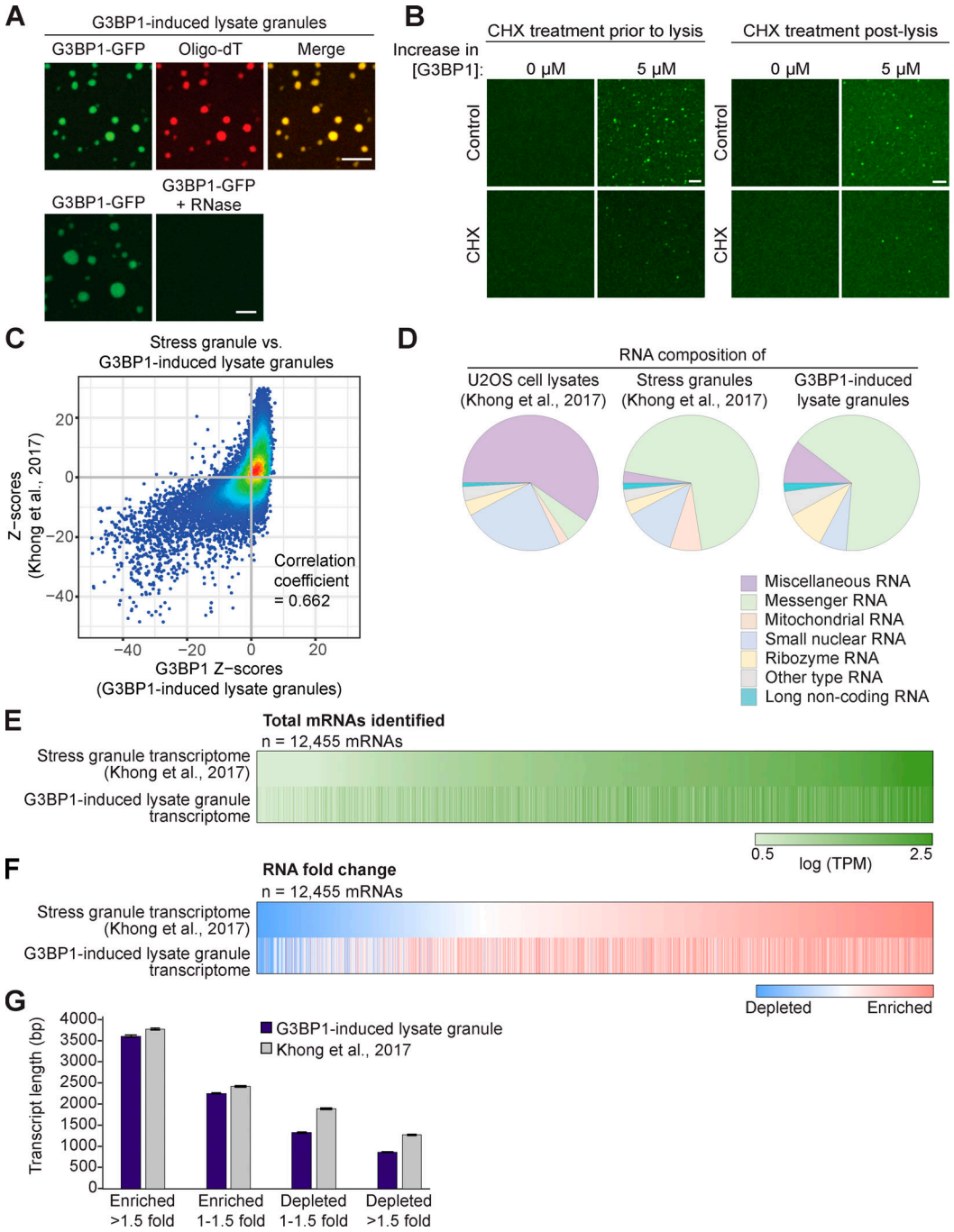

Figure 3. **The RNA composition of G3BP1-induced lysate granules resembles the RNA composition of stress granules in cells. (A)** Granules induced by increasing G3BP1 concentration by 20 μM incorporated labeled oligo-dT RNA (top). The addition of RNase (100 μg/ml) prevented the formation of granules (bottom). Images were obtained 30 min following induction with purified G3BP1. Scale bars, 10 μm. **(B)** U2OS cells stably expressing G3BP1-GFP were treated with 200 μg/ml cycloheximide (CHX) for 3 h before or immediately following lysis and the induction of lysate granules by increasing the concentration of G3BP1 by 5 μM using purified G3BP1. Images were obtained 30 min following induction with G3BP1. Scale bars, 5 μm. **(C)** G3BP1 lysate granule Z-scores (granule vs. lysate, x axis) were plotted against stress granule Z-scores (granule vs. lysate, y axis) to compare similarity in differentially expressed genes between lysate and stress granules (Khong et al., 2017) and were found to be highly similar. Pearson's correlation analysis (r = 0.662). **(D)** RNA composition of whole cell lysates (left), stress granules (middle), and lysate granules (right) analyzed by RNA-seq. Both stress granules and G3BP1-induced lysate granules primarily contain mRNA compared with the lysate from which they were derived. The RNA composition of G3BP1-induced lysate granules is highly similar to the published stress granule transcriptome (Khong et al., 2017). **(E)** Individual mRNAs identified in both the stress granule transcriptome (Khong et al., 2017) and G3BP1-induced lysate granules were color-coded from the most prevalent to the least prevalent within the granule. Log(TPM) was used for color coding such that mRNAs with log(TPM) ≤ 0.5 were assigned the lightest shade of green, whereas mRNAs with log(TPM) ≥ 2.50 were assigned the darkest shade of green. **(F)** mRNAs that were identified in both the stress granule transcriptome (Khong et al., 2017) and G3BP1-induced lysate granules were rank ordered from the most depleted (blue) to the most enriched (red) within the granule compared with their respective lysates. **(G)** Average mRNA transcript length is positively correlated with the level of granule enrichment or depletion in both stress granules and lysate granules. Graph represents mean ± SEM. n = 6,148, 5,604 (lysate granule, stress granule) for RNAs enriched >1.5-fold; n = 4,414, 2,701 (lysate granule, stress granule) for RNAs enriched 1–1.5-fold; n = 1,004, 2,047 (lysate granule, stress granule) for RNAs depleted 1–1.5-fold; and n = 889, 2,099 (lysate granule, stress granule) for RNAs depleted >1.5-fold.

by pretreatment of cultured cells before lysis or by supplementation with cycloheximide immediately after lysis (Fig. 3 B), demonstrating that G3BP1-induced stress granules in lysate are similarly dependent upon polysome disassembly.

We next performed RNA sequencing (RNA-seq) to comprehensively assess the RNA composition of lysate granules, using RNA isolated from lysates before induction with G3BP1 as a control. We compared these datasets with the RNA-seq results from a previously published study of the stress granule transcriptome (Khong et al., 2017; Table S2). We found strong similarity in the RNA transcriptomes of lysate granules and stress granules assembled in cells (Fig. 3 C and Table S3). Moreover, we found strong similarity in the classes of RNAs enriched in lysate granules and stress granules assembled in cells. Specifically, the transcriptomes of both lysate granules and stress granules were highly enriched in mRNAs and, to a lesser extent, in various classes of noncoding RNAs such as long non-coding RNA and pseudogene RNAs (Fig. 3 D and Table S3). One notable difference was an enrichment for mitochondrial RNAs in stress granules assembled in cells that was not present in lysate granules (Fig. 3 D and Table S3). This could represent a true difference in composition between lysate granules and stress granules assembled in cells; alternatively, it is possible that this reflects copurification of mitochondria with stress granules during isolation from intact cells. The lysate granules also contained a greater quantity of miscellaneous RNA and ribozyme RNA than stress granules, although these RNAs were still strongly depleted relative to control, as also observed with stress granules assembled in cells (Fig. 3 D and Table S3).

Our RNA-seq analysis identified >12,000 specific mRNAs within lysate granules, of which nearly all (>99.7%) were also found in the stress granule transcriptome (Khong et al., 2017). To visualize the similarity between these two datasets at the level of individual mRNAs, we generated a heat map that rank ordered mRNAs from the least prevalent to the most prevalent within the stress granule proteome, revealing a strong correlation between the mRNA composition of stress granules and lysate granules (Fig. 3 E). When these same mRNAs were analyzed according to depletion or enrichment in granules compared with the respective lysates from which they were derived, the heat maps were strikingly similar (Fig. 3 F).

Previous analysis of the stress granule transcriptome (Khong et al., 2017) and studies of LLPS driven by G3BP1 and RNA (Yang et al., 2020) have also revealed that mRNA length is an important feature of mRNA that drives LLPS and recruitment into stress granules. Indeed, we found a strong similarity in the relationship between depletion/enrichment and transcript length when we compared the transcriptomes of stress granules and lysate granules (Fig. 3 G). Altogether, these analyses demonstrate that granule assembly leads to enrichment in the same classes of RNA as well as RNA with similar features, irrespective of whether granules are seeded by G3BP1 in lysate or assembled in response to stress in cells. Thus, lysate granules faithfully recapitulate the RNA composition of stress granules assembled in cells.

Addition of exogenous NPM1 induces a distinct lysate granule

G3BP1 is the protein of highest centrality within the stress granule network and, as such, plays an outsized role in establishing the composition, and therefore the identity, of stress granules (Guillén-Boixet et al., 2020; Sanders et al., 2020; Yang et al., 2020; Zhang et al., 2019). Other proteins have been implicated as perhaps playing a similar critical role in the assembly of other biomolecular condensates. For example, NPM1 is an RNA-binding protein that occupies a central position in the network of interactions that underlies formation of the liquid, granular component of the nucleolus (Mitrea et al., 2016). Indeed, analogous to G3BP1, NPM1 oligomers undergo LLPS when mixed with nucleolar proteins and ribosomal RNAs (rRNAs; Mitrea et al., 2016). Thus, we hypothesized that recombinant, purified NPM1 might induce distinct biomolecular condensation in cellular lysate—namely, the liquid, granular component of the nucleolus.

NPM1 is a particularly abundant protein, and the endogenous protein was found to be present in U2OS cells at concentrations of ~7.7 μM (~0.7 μM in the cell lysate; Fig. S3 A). Supplementation of lysate with recombinant, purified NPM1 resulted in concentration-dependent condensation when the concentration was increased by 5 μM, reflecting a threshold concentration of ~5.7 μM, approximately equal to the endogenous NPM1 protein concentration (Fig. 4 A). When lysates generated from cells expressing either GFP or GFP-NPM1 were used to induce lysate granules, GFP was excluded from NPM1-induced lysate granules whereas GFP-NPM1 was targeted to the NPM1-induced lysate granules (Fig. 4 B and Fig. S3 B). The dynamic exchange of NPM1 in these lysate granules closely matched the rate of NPM1 dynamic exchange in nucleoli of intact cells as measured by FRAP (Fig. 4, B and C; and Video 6). Importantly, these NPM1-induced granules are distinct from G3BP1-induced granules. For example, in contrast to the potent inhibition of G3BP1-induced granules by the addition of viral nsP3 peptide, the formation of NPM1-induced granules was unaffected by the addition of nsP3 (Fig. 4 D), demonstrating that assembly of NPM1-induced granules does not require LLPS of G3BP1.

Next, we sought to characterize the protein composition of NPM1-induced lysate granules and compare this with the composition of nucleoli in cells as well as in G3BP1-induced lysate granules. As before, we began by interrogating the protein composition of lysate granules using an indirect immunofluorescence approach. Remarkably, nucleolin, a marker enriched in nucleoli but not stress granules, was strongly recruited to NPM1-induced granules but not G3BP1-induced granules (Fig. 4 E). In contrast, PABPC1 and TDP-43, which are found in stress granules but not nucleoli, were strongly recruited to G3BP1-induced granules but not NPM1-induced granules (Fig. 4 E). Finally, DDX21, which is a constituent of both stress granules and nucleoli, was found in lysate granules induced by either G3BP1 or NPM1 (Fig. 4 E).

We next performed a comprehensive analysis of proteins recruited to NPM1-induced granules using mass spectrometry (Table S4). Remarkably, gene ontology analysis of the NPM1-induced granule proteome revealed strong enrichment of nucleolar components (Fig. 4 F). Notably, the proteome of NPM1-induced granules shared some features of the G3BP1-induced granule proteome, including enrichment of proteins with ATPase activity, helicase activity, and RNP components, which are

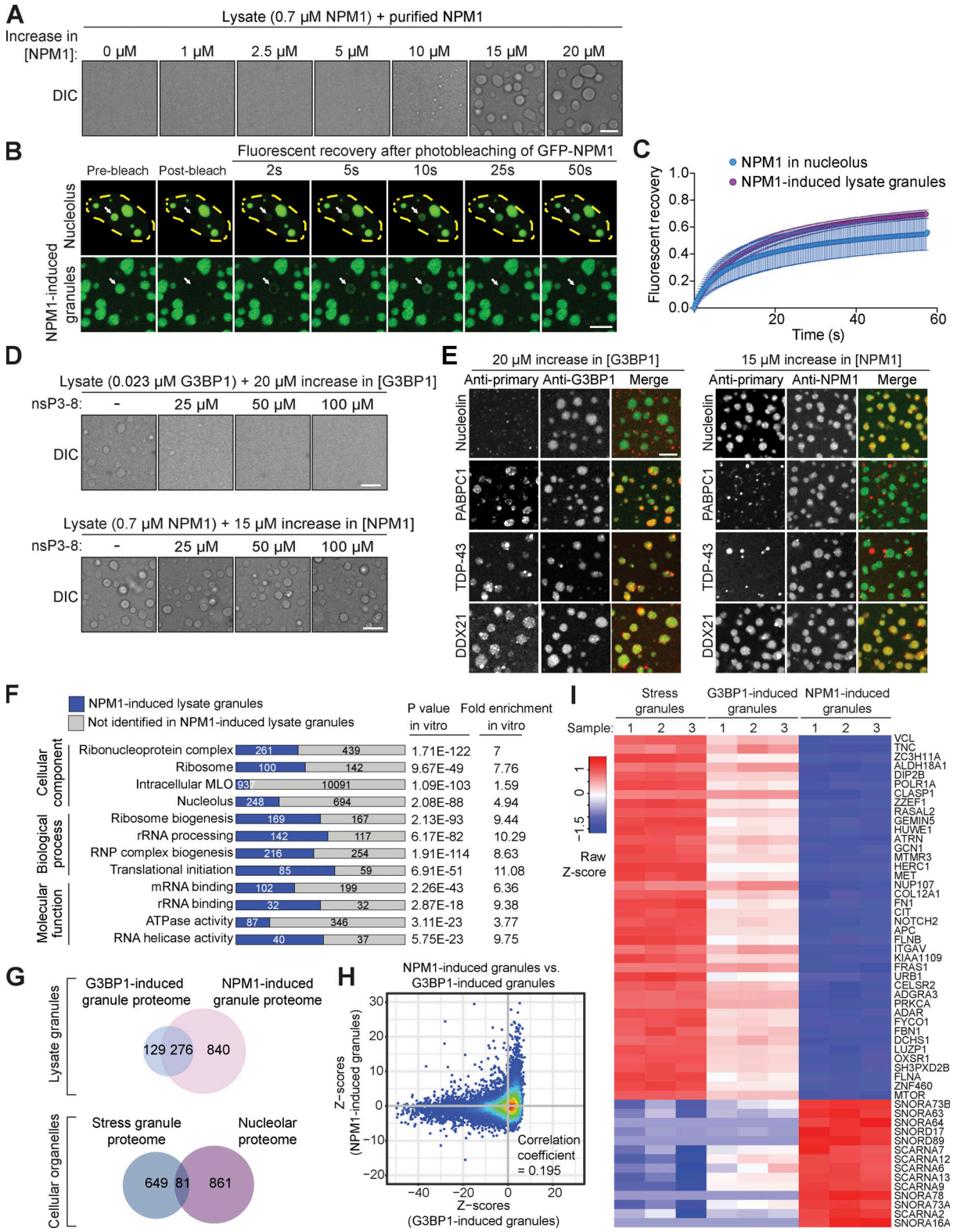

Figure 4. **Addition of NPM1 to a cell lysate induces a distinct lysate granule that recapitulates the composition and properties of the nucleolus. (A)** Addition of purified NPM1 protein to a cell lysate induces LLPS in a dose-dependent manner when the concentration of NPM1 is increased by more than 5 μM. Scale bar, 10 μm. **(B and C)** FRAP performed on cells or lysate from cells transiently expressing GFP-NPM1 shows similar mobility between the nucleolar NPM1 in intact U2OS cells and NPM1 in lysate granules induced by increasing the concentration of NPM1 by 15 μM using purified NPM1. White arrows indicate nucleolus or NPM1 lysate granule on which FRAP was performed. Nuclear boundary is indicated by yellow dashed line. All images were acquired 30 min after induction. Scale bar, 10 μm, n = 10 granules from either cells or lysate. Graph represents mean ± SD. **(D)** The nsP3-8 peptide from Chikungunya virus strongly inhibits the formation of G3BP1-induced lysate granules (top) but has no effect on the formation of NPM1-induced lysate granules (bottom). Scale bars, 10 μm.

(E) Indicated primary antibodies were conjugated with Alexa Fluor 647 secondary, and either anti-G3BP1 or anti-NPM1 was conjugated with Alexa Fluor 488 secondary. Conjugated antibodies were added to U2OS lysates along with purified G3BP1 or NPM1. Scale bar, 10 µm. **(F)** Gene ontology (GO) analysis of proteins found to be enriched within NPM1-induced (increasing NPM1 concentration by 15 µM) lysate granules by mass spectrometry reveals that lysate granules show nucleolar features as well as some common features with G3BP1-induced (increasing G3BP1 concentration by 20 µM) lysate granules. MLO, membraneless organelle. **(G)** Venn diagrams showing the overlap of proteins identified through mass spectrometry between NPM1-induced lysate granules (increasing NPM1 concentration by 15 µM) and G3BP1-induced lysate granules (increasing G3BP1 concentration by 20 µM), as well as the overlap of proteins previously identified in stress granules (RNA Granule Database, see main text) and the nucleolar proteome as assessed by GO analysis of the PANTHER database. **(H)** G3BP1 lysate granule Z-scores (granule vs. lysate, x axis) were plotted against NPM1 lysate granule Z-scores (granule vs. lysate, y axis) to compare similarity in differentially expressed genes between G3BP1 and NPM1 lysate granules and were found to be highly dissimilar. Pearson's correlation analysis (r = 0.195). **(I)** Heat map of the gene expression of the enriched RNAs (relative to their own control total cellular RNA or total lysate) in stress granules (Khong et al., 2017), G3BP1 lysate granules, and NPM1 lysate granules.

typical constituents of many RNP granules in cells (Fig. 4 F). This overlap was reflected in 276 specific proteins that were found in the proteomes of both NPM1-induced granules and G3BP1-induced granules (Fig. 4 G), a compositional overlap that mirrors that observed between stress granules and nucleoli in cells. We also noted that the NPM1-induced lysate granule proteome was substantially larger than that of the G3BP1-induced lysate granule proteome, again mirroring the relative complexities of the nucleolus versus stress granules in cells (Fig. 4 G).

We next performed RNA-seq to assess the RNA component of NPM1-induced lysate granules, using RNA isolated from lysates before induction with NPM1 as a control. Whereas the NPM1-induced lysate granules were enriched in a subset of lysate RNAs, there was virtually no correlation with the RNAs enriched by G3BP1-induced lysate granules (Figs. 4 H and S3 C; and Table S5). Whereas G3BP1-induced lysate granules were strongly enriched with mRNA from the lysate (Fig. 3 D), NPM1-induced granules were depleted of mRNA and enriched in nuclear RNAs, including noncoding RNAs that are known to localize to the nucleolus (Fig. 4 I, Table S3, and Table S5). Small nucleolar RNAs (snoRNAs) are a tiny fraction of RNA found within whole cell lysates but are strongly concentrated within the nucleolus, where they function primarily to guide the maturation of ribosome biogenesis (Ojha et al., 2020). The targeting of snoRNAs to the nucleolus was strongly recapitulated with the NPM1-induced lysate granules, whereas snoRNAs were largely absent in G3BP1-induced lysate granules and stress granules (Fig. 4 I). Ribozyme RNA was enriched more than fourfold within the NPM1 lysate granule, driven almost entirely by a single ribozyme transcript, *RMRP*, that represented >30% of the transcripts identified through RNA-seq (Fig. S3 C and Table S5). The primary cellular localization of *RMRP* is within the nucleolus, where it functions in pre-ribosomal RNA processing (Martin and Li, 2007). Altogether, analyses of NPM1-induced lysate granules revealed a protein and RNA composition distinct from that of G3BP1-induced lysate granules, recapitulating features of the granular component of the nucleolus. These results further illustrate that it is possible to faithfully recapitulate distinct RNP granules, and likely other biomolecular condensates, in whole cell lysate.

Discussion

This study describes faithful recapitulation of two different types of RNP granules within a highly tractable cell lysate system. This system is a valuable tool for studying the biology of RNP granules and bridges the gap between live cells and simple in vitro systems consisting of just a few purified components. This tool also provides novel insight into the mechanism whereby condensates establish and maintain distinct compositions. Indeed, the central observation that stress granules were reconstituted within cellular lysate by increasing the concentration of a single protein, G3BP1, fulfilled several predictions that arose from earlier work.

RNP granules arise by LLPS. We now appreciate that the percolation threshold for LLPS in RNP granule assembly is encoded by the network of weak, transient protein–protein, protein–RNA, and RNA–RNA interactions (Guillén-Boixet et al., 2020; Sanders et al., 2020; Yang et al., 2020). Each component of this network contributes toward the sum of interactions necessary to breach the percolation threshold. Importantly, however, some components contribute more than others. The contribution of individual proteins to stress granule assembly has been assessed by unbiased, whole-genome genetic screening (Yang et al., 2020). Moreover, the network of interactions underlying stress granule assembly in U2OS cells has now been elucidated based on stress granule proteomics (Jain et al., 2016; Markmiller et al., 2018; Youn et al., 2019). Integration of the genetic screen results with the network of interactions has found a correlation between a protein's centrality within the stress granule network and its importance in stress granule assembly (Yang et al., 2020). On this basis, it has been suggested that one could manipulate individual stress granule proteins with predictable outcomes (Yang et al., 2020). One illustration of this concept is the well-appreciated phenomenon whereby overexpression of some stress granule proteins in cells is sufficient to trigger condensation in the absence of exogenous stress (Kedersha et al., 2016; Sanders et al., 2020).

The most central nodes in the stress granule interaction network—predicted to lend the greatest contribution to stress granules assembly—are G3BP1 and G3BP2 (Yang et al., 2020). Consistent with this finding was the earlier observation that double knockout of *G3BP1* and *G3BP2* prevents stress granule assembly in response to arsenite (Kedersha et al., 2016). The importance of G3BP1 in stress granule assembly has also been shown in an optogenetic system in which light-induced LLPS of G3BP1 in cells was sufficient to drive the formation of stress granules even in the absence of exogenous stress (Zhang et al., 2019). This is not a feature of any stress granule protein, since light-induced LLPS of TIA1, FUS, or TDP-43 does not trigger

stress granule assembly (Zhang et al., 2019). Thus, the ability to trigger stress granule assembly in lysate by supplementation with purified G3BP1 (but not other proteins such as BSA or hnRNPA1) fulfills a prediction built on a wealth of recent in vitro and cell-based studies. Moreover, the likely generalizability of this phenomenon is illustrated by the finding that increasing the concentration of NPM1 created a distinct condensate that recapitulates features of the nucleolar granular component, consistent with the central role of NPM1 in the network of interactions constituting this distinct condensate in cells. These findings are also consistent with a recent study using yeast lysate, in which the addition of specific mRNAs was sufficient to trigger the formation of structures that feature characteristics of stress granules (Begovich and Wilhelm, 2020). The extent to which supplementation of lysates with RNAs can fully recapitulate stress granules or other RNP granule types awaits in-depth analysis of composition through methods such as proteomics and RNA-seq.

Moreover, it has been previously suggested that cells, and in particular dynamic structures such as RNP granules, are self-organizing systems whose principles of organization are determined by the intrinsic properties of the components of each structure (Misteli, 2001; Misteli, 2008). Until recently, however, there have been few ways in which this concept has been experimentally testable. Our results serve as a dramatic illustration of these self-organizing principles while also providing a useful tool for studying biomolecular condensation in general. Indeed, this system allows investigators to exploit insights into the logic that underlies the network-encoded percolation threshold for many different types of condensates. With foreknowledge of the network underlying a condensate, as well as the centrality of each node within the network, one can predict how to construct an individual condensate within a lysate—namely, by using the central constituent to breach the percolation threshold and trigger the formation of a condensate with a specific composition. Within this lysate system, it is possible to identify causal relationships between experimental manipulations and changes in granule properties independent of potentially confounding signaling pathways occurring within cells. These manipulations could include fine-tuning specific properties (e.g., salt, pH) of the milieu in which the condensates form or genetically modifying specific constituents by introducing mutations. These mutations could be designed to interrogate the function of a specific constituent or, importantly, could replicate a disease context. Indeed, understanding precisely how disease-causing mutations lead to changes in material properties of specific condensates remains one of the most vital unanswered questions in the field of neurodegeneration and ALS/frontotemporal dementia in particular.

We propose that this system could be used to study the role of biomolecular condensation in disease as well as the identification of small molecules to reverse pathological phase transitions. The impact of cycloheximide or the nsP3 peptide on granule formation provides a blueprint for how small molecules can be screened by either pretreating cells before lysis or by the addition of a compound directly to the lysate. For example, substantial evidence has accrued to suggest that pathological phase transitions are primary drivers of disease, such as *EWSR1/FL1* translocations in Ewing's sarcoma and dynamical arrest of stress granules in ALS (Mathieu et al., 2020). Substantial effort is underway to identify small molecules that prevent or reverse these pathological phase transitions, and the system described here will be useful in these endeavors. These efforts frequently rely upon simple in vitro systems that reconstitute LLPS of a few constituents. Whereas such systems permit exquisite control over the experimental conditions, cellular context is missing, including most native constituents and the enzymes that conduct regulation of biomolecular condensation. Alternatively, monitoring of biomolecular condensation in intact cells can be used to capture greater complexity. However, precise control of concentrations is difficult in intact cells, which are also impermeable to many small molecules that arise from high-throughput screens. Cell-based platforms can also be confounded by off-target cytotoxicity. The lysate system described here represents a valuable bridge between these systems and complements the weaknesses of each.

The manner in which lysate granules settle on the surface of imaging chambers may afford another advantage by allowing examination of granule substructures using advanced imaging techniques, including super-resolution microscopy. Moreover, as the system is highly tractable, manipulations can be made to the lysate (e.g., small molecules, temperature, altering concentrations of individual constituents) in real time, allowing the assessment of specific variables on granule dynamics and maturation and enabling deeper understanding of the relationship between complex networks and condensate properties.

Materials and methods

Constructs

EGFP–Caprin-1 was inserted in frame with GFP into the eGFP-C3 vector between the *SacI* and *EcoRI* restriction sites (Yang et al., 2020). GFP-NPM1 and GFP-FUS were purchased from Addgene (17578, 98651). For EGFP-C1-hnRNPA1, hnRNPA1 was inserted into the eGFP-C1 vector with *BamHI* and *XbaI* restriction sites used for cloning.

Cell culture and transfection

U2OS cells were purchased from American Type Culture Collection (HTB-96). Cells were cultured in DMEM (HyClone) supplemented with 10% FBS (HyClone; SH30071.03 and SH30396.03) and maintained at 37°C in a humidified incubator with 5% CO_2. Lipofectamine 2000 (Thermo Fisher Scientific; 11668019) for U2OS cells was used for transient transfections according to the manufacturer's instructions. U2OS cells stably expressing G3BP1-GFP or GFP were generated by lentiviral transduction of a pCLi40w-MND-G3BP1-GFP plasmid (Figley et al., 2014).

Cycloheximide treatment

For prelysis cycloheximide experiments, either 200 µg/ml cycloheximide (Sigma; C7698-1G, reconstituted in ethanol) or an equal volume of ethanol as a control was treated to G3BP1-GFP cells for 3 h before harvesting cells for use in lysate LLPS

experiments. Protein content between samples was equalized for lysate LLPS experiments. For postlysis cycloheximide experiments, G3BP1-GFP cell pellets were lysed in lysis buffer containing either 200 µg/ml cycloheximide (C7698-1G, reconstituted in double-distilled water (ddH_2O) or an equal volume of ddH_2O.

Generation of knock-in (KI) cell lines

Genetically modified U2OS cells were generated using CRISPR-Cas9 technology. Briefly, 400,000 U2OS cells were transiently cotransfected with 200 ng gRNA expression plasmid (cloned into Addgene 43860), 500 ng Cas9 expression plasmid (Addgene; 43945), 200 ng pMaxGFP, and 500 ng donor plasmid via nucleofection (Lonza; 4D-Nucleofector X-unit) using solution P3, program CM-104 in small cuvettes according to the manufacturer's recommended protocol. Cells were single-cell sorted by FACS to enrich for GFP^+ (transfected) cells, clonally selected, and verified for the desired targeted modification via PCR-based assays and targeted deep sequencing.

Preparation for lysis

To prepare cells for use in in vitro lysate LLPS, cells were grown to confluency in 10-cm cell culture–treated dishes (Corning; 430293). To harvest cells, medium was aspirated and cells were washed with PBS. 5 ml PBS was added following the wash, and cells were scraped to detach. After detachment, cells were centrifuged at 500 *g* for 3 min. PBS was removed by aspiration, leaving the cell pellet untouched. Cell pellets were stored at −80°C for up to 3 mo.

Determination of nuclear lysis

To determine nuclear lysis, 2 µg/ml Hoechst (Biotium; 40046) was added to buffer (ddH_2O, 50 mM Tris-HCl, pH 7.0, and protease inhibitor cocktail; Roche) supplemented with 2.5% murine RNase inhibitor (New England Biolabs; M0314) with or without 0.5% NP-40. Cell pellets were resuspended or lysed in either buffer by gently pipetting up and down 5–10 times using 1,000-µl pipette tips until the cells formed a homogenate in the buffer, transferred to an Eppendorf tube, and incubated at room temperature for 8 min. Samples were then rehomogenized by gently pipetting up and down three times to ensure an even distribution of nuclei, followed by seeding in a µ-Slide Angiogenesis with ibiTreat (Ibidi; 81506) to observe the amount of intact nuclei. Imaging was performed at room temperature using a Yokogawa CSU W1 spinning disk attached to a Nikon Ti2 eclipse with a Photometrics Prime 95B camera using Nikon Elements software (version 5.21.02). Imaging was performed through a Nikon Plan Apo 20× 0.75 NA dry objective using a 405-nm laser. Automated nuclei detection and measurement were performed using CellProfiler software (Broad Institute) similar to the methods described previously (Mackenzie et al., 2017), segmenting nuclei rather than stress granules. Briefly, the nuclei were segmented by applying a global "minimum cross entropy" approach on the 405 channel. The sizes represent an average of three separate fields, with each field containing at least 100 segmented nuclei.

Western blotting

4X NuPAGE lithium dodecyl sulfate sample buffer (Thermo Fisher Scientific; NP0008) with 1% SDS was added to lysate, pellet, or purified G3BP1 diluted in lysis buffer or purified NPM1 diluted in lysis buffer, and samples were boiled at 70°C for 5 min. Samples were separated by SDS-PAGE and transferred to membranes. Western blots were performed with anti-G3BP1 (mouse; BD Biosciences; 611127), anti-NPM1 (mouse; Sigma; B0556), or anti-actin (goat; Santa Cruz Biotechnology; sc-1616-R) at 4°C overnight. Membranes were washed three times with PBST (0.1% Tween) and further incubated with dye-labeled secondary antibodies (donkey anti-mouse IRDye 800CW; LI-COR; 926–32212; and donkey anti-goat IRDye 680RD; LI-COR; 926–68074). Membranes were visualized with an Odyssey Fc imaging system (LI-COR).

Protein purification

hnRNPA1 full-length (Molliex et al., 2015) and G3BP1 full-length (Yang et al., 2020) and mutants were expressed and purified from *Escherichia coli* BL21-Gold (DE3) cells (Agilent) or Rosetta 2(DE3) cells (Millipore), respectively. hnRNPA1 full-length protein was expressed as His-SUMO–tagged fusion proteins, whereas G3BP1 was expressed as GST/6×-His fusion proteins. *E. coli* was grown to OD_{600} of 0.8 and induced with 0.6 mM IPTG at 16°C overnight. Cells were then pelleted and resuspended in lysis buffer containing 50 mM Hepes, pH 7.5, 250 mM NaCl, 30 mM imidazole, 2 mM βME, 100 µg/ml RNase, and complete protease inhibitor cocktail for hnRNPA1 and 250 mM NaCl, 50 mM Hepes 7.5, 1 mM DTT, protease inhibitor, and 20 mM imidazole for G3BP1 full-length and mutants. After sonication, lysates were pelleted at 17,000 *g* at 4°C for 45 min, and supernatant was loaded onto a gravity nickel-nitrilotriacetic acid column, washed with lysis buffer, and eluted with increasing concentrations of imidazole (up to 500 mM) on an AKTA pure system. The proteins were further treated with 0.1 mg/ml RNase A (Thermo Fisher Scientific; EN0531) to remove RNA. G3BP1 proteins were treated with tobacco etch virus protease (Sigma; T4455) overnight at room temperature to cleave both GST and 6×-His tags. Cleaved proteins were further purified by ion exchange with a HiTrap SP or Q column. The fractions were analyzed by SDS-PAGE, pooled, and concentrated. The proteins were then purified by Superdex 200 16/200 column (GE) equilibrated in size exclusion chromatography buffer (400 mM NaCl, 50 mM Hepes 7.5, and 1 mM DTT). The fractions were analyzed by SDS-PAGE, pooled, concentrated, filtered, flash frozen in liquid nitrogen, and stored at −80°C. Purified recombinant NPM1 was received as a gift from the Kriwacki Lab (St. Jude Children's Research Hospital, Memphis, TN). BSA was purchased from Sigma.

Peptide synthesis

The nsP3_8 WT peptide (LTFGDFDE) was synthesized by the Hartwell Center for Bioinformatics and Biotechnology at St. Jude Children's Research Hospital, Molecular Synthesis Resource, using standard solid-phase peptide synthesis chemistry. The peptide was reconstituted from lyophilized form into DMSO or lysis buffer (ddH_2O, 50 mM Tris-HCl, pH 7.0, and 0.5% NP-40) for experimental use with the two-component LLPS or lysate systems, respectively.

LLPS of purified G3BP1 and RNA

LLPS of purified G3BP1 WT or mutant at the indicated concentration was induced by addition of 200 ng/ml RNA. The samples

were mixed in low binding tubes (COSTAR; 3206) and transferred to a sandwiched chamber created by a cover glass and a glass slide with a double-sided spacer (Sigma; GBL654002). Samples were observed by DIC using a Leica DMi8 wide-field microscope with EL6000 excitation light source with a mercury halide lamp and a Hamamatsu Orca Flash 4.0 V2 camera using LAS X software (Leica; Version 3.7.1). Images were acquired through an HC Plan Apo 20× 0.8 NA dry objective. All images were captured at room temperature within 5 min after LLPS induction. The buffer for LLPS contained 150 mM NaCl and 50 mM Hepes, pH 7.5. Total RNA was isolated from U2OS cells using TRIzol (Thermo Fisher Scientific), and the concentration of RNA was measured by NanoDrop (Thermo Fisher Scientific). For nsP3_8 peptide experiments, the peptide was mixed with G3BP1 before the addition of RNA.

Cell lysis and induction of LLPS from lysate

Cell pellets were removed from −80°C and thawed at room temperature for 2 min. 250 µl lysis buffer (ddH_2O, 50 mM Tris-HCl, pH 7.0, 0.5% NP-40, and protease inhibitor cocktail; Roche) supplemented with 2.5% murine RNase inhibitor (New England Biolabs; M0314; not included when RNase was used) was added to each pellet. The cell pellet was lysed in the buffer by gently pipetting up and down 5–10 times using 1,000-µl pipette tips until the cells formed a homogenate in the buffer, transferred to an Eppendorf tube, and incubated at room temperature for 3 min. Lysates were then centrifuged at room temperature for 5 min at 21,000 *g*. Lysate supernatants were transferred to a new Eppendorf tube and combined with purified protein to induce LLPS along with any other exogenous reagents used in the experiment. Immediately after mixing, samples were seeded into imaging vessels to observe LLPS. The following imaging vessels were used, including corresponding volumes seeded per well: 20 µl in µ-Slide Angiogenesis with ibiTreat; 125 µl in eight-well laboratory-Tek chambered cover glass (Nunc); or 20 µl in 384-well glass bottom SensoPlate (Greiner). All experiments that were quantified were performed in eight-well Lab-Tek slides; otherwise, Ibidi slides were used. The 384-well plate was only used for the multidimensional phase diagram (Fig. 1, H and I). Since temperature is known to influence LLPS of many low-complexity domain–containing proteins, all manipulations and analysis following lysis were performed at room temperature (22°C–25°C).

Fluorescent microscopy and image analysis

Fluorescent imaging was performed at room temperature using a Yokogawa CSU W1 spinning disk attached to a Nikon Ti2 eclipse with a Photometrics Prime 95B camera using Nikon Elements software (versions 5.20.00 to 5.21.02). Imaging was performed through a Nikon Plan Apo 60× 1.40 NA oil objective with Immersol 518 F (Zeiss; refractive index 1.518), and Perfect Focus 2.0 (Nikon) was engaged for all captures. For single time point captures using the Ibidi Angiogenesis slides, images were taken at the surface of the sample at 30 min after induction or at the indicated time point. Imaging was performed using 488-nm, 555-nm, and 640-nm lasers when applicable along with a capture of DIC. Multipoint time-lapse imaging was performed in Lab-Tek chambered cover glass slides, where 5 xy fields were stored for each condition. Images were taken at each xy position every 10 min. Automated granule detection and measurement were performed using CellProfiler software similar to the methods described previously (Mackenzie et al., 2017), excluding association of granules to cells. Briefly, the lysate granules were segmented by applying a global minimum cross entropy approach on the GFP channel. The sizes represent an average of at least five separate fields, with each field containing at least 100 segmented granules.

Multidimensional phase diagram

Lysates at indicated concentrations combined with indicated concentrations of G3BP1 were seeded into a 384-well glass-bottom SensoPlate at 20 µl per well. Imaging was performed on a Cytation 5 multi-mode imaging plate reader (BioTek) equipped with a Sony IMX 264 camera using Gen5 software (BioTek; version 3.08.01). Images were acquired through an Olympus Plan Fluorite 40× Phase 0.6 NA dry objective, captured at room temperature through transmitted light 60 min after induction.

Antibody preparation and reagents added exogenously to lysate

Addition of all exogenous reagents, with the exception of 1,6-hexanediol, occurred simultaneously with the addition of purified G3BP1. Dilutions of reagents were performed in lysis buffer whenever possible. The following antibodies were used: anti-actin (goat; Santa Cruz Biotechnology; sc-1616-R), anti-DCP1a (rabbit; Abcam; ab47811), anti-FKBP12 (rabbit; Santa Cruz Biotechnology; sc-28814), anti-TOM20 (rabbit; Santa Cruz Biotechnology; sc-11415), anti-GOLGA3 (rabbit; Santa Cruz Biotechnology; sc-292192), anti-CAPRIN1 (rabbit; Proteintech; 15112–1-AP), anti-PABPC1 (rabbit; Abcam; ab21060), anti-PRRC2C (rabbit; Abcam; ab117790), anti-USP10 (rabbit; Proteintech; 19374–1-AP), anti-UBAP2L (rabbit; Abcam; ab138309), anti-CSDE (rabbit; Bethyl Laboratories; A303-158A), anti-DDX21 (rabbit; Novus; NB100-1718SS), anti-NPM1 (mouse; Sigma; B0556), anti-nucleolin (rabbit; Abcam; ab22758), anti-G3BP1 (mouse; BD Biosciences; 611127), anti-TDP43 (rabbit; Proteintech; 12892–1-AP), Alexa Fluor 647 (donkey anti-rabbit; Life Technologies; A31573), Alexa Fluor 647 (donkey anti-mouse; Life Technologies; A31571), Alexa Fluor 488 (donkey anti-mouse; Life Technologies; A21202), and Alexa Fluor 647 (donkey anti-goat; Life Technologies; A21447). For use in lysate LLPS experiments, primary and secondary antibodies were diluted in lysate buffer and combined to preconjugate for 1 h at room temperature on an orbital shaker at the lowest speed setting, before being added to lysate alongside purified protein. Total dilutions were 1:1,000 for secondary antibodies; primary antibody dilutions were identical to the manufacturers' recommendation for immunofluorescence/immunohistochemistry. Oligo-DT labeled with Cy5 (Genelink; 26–4320-02) and RNase were obtained from Thermo Fisher Scientific (EN0531). 1,6-hexanediol (Sigma; H11807-500G) was added to lysate granules in the imaging vessel at a final concentration of 10% either 15 or 30 min after initial granule formation. Samples were gently pipetted up and down three times to ensure thorough mixing.

FRAP

FRAP experiments were performed on a Yokogawa CSU W1 spinning disk attached to a Nikon Ti2 eclipse with a Photometrics Prime 95B camera using Nikon Elements software (versions 5.20.00 to 5.21.02). The light path was split between the port for the spinning disk/acquisition laser and the FRAP lasers, enabling FRAP to occur simultaneously while imaging. All FRAP imaging was taken on a Nikon Plan Apo 60× 1.40 NA oil objective, with Immersol 518 F/37C (Zeiss; refractive index 1.518) for live-cell imaging or Immersol 518 F (Zeiss; refractive index 1.518) for lysate granules, with Perfect Focus 2.0 engaged. For live-cell FRAP, cells were seeded into four-well Lab-Tek chambered cover glass (Nunc) with Fluorobrite DMEM media supplemented with 10% FBS and 4 mM L-glutamine. During imaging, cells were maintained at 37°C and supplied with 5% CO_2 using a Bold Line Cage Incubator (Okolabs) and an objective heater (Bioptechs).To induce stress granules, cells were incubated with 500 µM sodium arsenite (Sigma) for 30 min. FRAP of lysate granules occurred at room temperature with no supplemental CO_2. Time lapses were acquired as rapidly as possible over the course of 35 s for stress granules and G3BP1-induced granules and 60 s for nucleoli and NPM1-induced granules, with photobleaching with the 488-nm FRAP laser occurring 2 s into capture. Data were taken from at least n = 10 different cells or lysate granules for each condition. In Nikon Elements, regions of interest were generated in the photobleached region, a non-photobleached cell, and the background for each time lapse, and the mean intensity of each was extracted. These values were exported into Igor Pro 7.0 (WaveMetrics), where photobleach and background correction were performed, and fit FRAP curves were generated.

Measurement of protein concentration

To measure the protein content of lysates, Bradford assays were run on lysate supernatants against BSA standards. To measure the total protein content of cells to equalize lysate concentrations in LLPS experiments, 10% of each cell pellet was reserved before freezing and lysed in equal volume 2× lysis buffer (ddH_2O, 100 mM Tris-HCl, pH 7.0, and 1% NP-40), and a Bradford assay was run against BSA standards. For LLPS experiments, the lowest concentrated samples were lysed in 225 µl lysis buffer (rather than the standard 250 µl), and the remaining samples were lysed in higher volumes to equalize protein content between samples.

LC-MS/MS

Lysate granules were induced as described above by increasing the concentration by either 20 µM (G3BP1) or by 15 µM (NPM1) or a mock purification as a control without addition of purified protein. Granules were allowed to form for 40 min, and granules were isolated from the lysate by centrifugation at 2,000 g for 5 min. The resulting granules were collected in 2× LDS sample buffer and separated by SDS-PAGE. Proteins were isolated from the gel and digested with trypsin overnight. Samples were loaded on a nanoscale capillary reverse-phase C18 column by an HPLC system (Thermo Ultimate 3000) and eluted by a gradient (~90 min). Eluted peptides were ionized by electrospray ionization and detected by an inline mass spectrometer (Thermo Orbitrap Fusion). Database searches were performed using SEQUEST search engine using an in-house SPIDERS software package. Tandem mass spectrometry spectra were filtered by mass accuracy and matching scores to reduce protein false discovery rate to ~1%. The total number of spectral counts for each protein identified was reported by sample. Proteins were included in the granule interactomes if they were found to be enriched at least twofold in the granule versus mock samples and had at least two separate peptides identified by LC-MS/MS.

RNA-seq

Lysate granules were induced by increasing the concentration of G3BP1 by 100 µM or NPM1 by 15 µM using purified G3BP1/NPM1 and were allowed to form for 40 min followed by granule isolation from the lysate by centrifugation at 2,000 g for 5 min. RNA was isolated from either the lysate immediately before induction with G3BP1 or from the isolated granules. Stranded total RNA was used for RNA-seq analysis in triplicate samples from RNA isolated from both lysate and granules as described below. RNA was quantified using the Quant-iT RiboGreen assay (Life Technologies) and quality checked by 2100 Bioanalyzer RNA 6000 Nano assay (Agilent Technologies), 4200 TapeStation High Sensitivity RNA ScreenTape assay (Agilent Technologies), or LabChip RNA Pico Sensitivity assay (PerkinElmer) before library generation. Libraries were prepared from total RNA with the TruSeq Stranded Total RNA Library Prep Kit according to the manufacturer's instructions (Illumina; PN 20020599). Libraries were analyzed for insert size distribution on a 2100 BioAnalyzer High Sensitivity kit (Agilent Technologies), 4200 TapeStation D1000 ScreenTape assay (Agilent Technologies), or Caliper LabChip GX DNA High Sensitivity Reagent Kit (PerkinElmer). Libraries were quantified using the Quant-iT PicoGreen ds DNA assay (Life Technologies) or low pass sequencing with a MiSeq nano kit (Illumina). Paired-end 100-cycle sequencing was performed on a NovaSeq 6000 (Illumina). For comparative analysis, RNAs that comprised >1 transcript per million (TPM) within the mRNA fraction of both the lysate and stress granules were used, representing >99.7% of the mRNAs identified from both lysate and stress granules. Differential expression analysis was performed with the limma and voom method in R, with raw read counts normalized by the TMM (trimmed mean of M values) method. Pairwise Pearson's correlation analysis was performed with the Z-scores from the differential expression analysis to compare the similarity and dissimilarity of stress granules, G3BP1 lysate granules, and NPM1 lysate granules relative to their own total cell or lysate RNA as control.

Statistics and graphs

The one-way ANOVA was calculated in GraphPad Prism. Data distribution was assumed to be normal, but this was not formally tested. Graphs for the analysis were made in Microsoft Excel and GraphPad Prism. All errors corresponding to the SD or standard error of the population are described in the figure legends. Statistically significant differences and the number of samples analyzed for each experiment are indicated in the figure legends.

Online supplemental material

Fig. S1 shows nuclear lysis before granule induction, the concentration of G3BP1 in the lysate before induction with purified protein, and dissolution of granules with 1,6-hexanediol. Fig. S2 shows representative images used in the quantitation of Fig. 2 C. Fig. S3 shows the concentration of NPM1 in the lysate and pellet before induction with purified protein and the exclusion of GFP from NPM1 lysate granules. Table S1 shows proteins identified in G3BP1 lysate granules by mass spectrometry. Table S2 shows RNA-seq data from G3BP1 lysate granules compared with stress granules. Table S3 shows the RNA composition by type of stress granules, G3BP1 lysate granules, and NPM1 lysate granules as assessed by RNA-seq. Table S4 shows proteins identified in NPM1 lysate granules by mass spectrometry. Table S5 shows the RNA composition by type of NPM1 lysate granules. Video 1 and Video 2 show formation, growth, and fusion of G3BP1-induced lysate granules at low and high power, respectively (related to Fig. 1). Video 3 shows the dynamics of G3BP1-induced lysate granules as assayed by FRAP (related to Fig. 1). Video 4 and Video 5 show conserved dynamics of cellular stress granules and G3BP1-induced lysate granules as assayed by FRAP (related to Fig. 2). Video 6 shows conserved dynamics of cellular nucleoli and NPM1-induced lysate granules as assayed by FRAP (related to Fig. 4). In all cases, videos of lysate granules are focused on condensates that have settled on the slide surface; videos of granules inside intact cells are focused on cells adhering to the surface of the imaging chamber.

Acknowledgments

We thank Natalia Nedelsky for editorial assistance. We thank the Center for Advanced Genome Engineering at St. Jude Children's Research Hospital for assistance with CRISPR-Cas9 modified cell lines, the Center for Proteomics and Metabolomics at St. Jude Children's Research Hospital for assistance with mass spectrometry analyses, and the Hartwell Center Genome Sequencing Facility for assistance with RNA-seq. We thank Gang Wu and Michael Wang for assistance with analyses of RNA sequencing data, Richard Kriwacki for sharing purified NPM1, and Jessica Hughes for assistance with protein preparation.

This work was supported by grants from the Howard Hughes Medical Institute, National Institutes of Health grant R35NS097974, the St. Jude Research Collaborative on Membraneless Organelles, and the ALS Association (18-IIA-419) to J.P. Taylor. The content is solely the responsibility of the authors and does not necessarily represent the official views of the National Institutes of Health.

J.P. Taylor is a consultant for Nido Biosciences and Faze Medicines. The authors declare no additional competing financial interests.

Author contributions: J.P. Taylor conceived and supervised the project. B.D. Freibaum, J. Messing, and P. Yang designed and/or performed the experiments. B.D. Freibaum, J. Messing, H.J. Kim, and J.P. Taylor analyzed data and wrote the manuscript.

Submitted: 14 September 2020
Revised: 9 December 2020
Accepted: 28 December 2020

References

Banani, S.F., H.O. Lee, A.A. Hyman, and M.K. Rosen. 2017. Biomolecular condensates: organizers of cellular biochemistry. *Nat. Rev. Mol. Cell Biol.* 18:285–298. https://doi.org/10.1038/nrm.2017.7

Begovich, K., and J.E. Wilhelm. 2020. An In Vitro Assembly System Identifies Roles for RNA Nucleation and ATP in Yeast Stress Granule Formation. *Mol. Cell.* 79:991–1007.E4. https://doi.org/10.1016/j.molcel.2020.07.017

Berry, J., S.C. Weber, N. Vaidya, M. Haataja, and C.P. Brangwynne. 2015. RNA transcription modulates phase transition-driven nuclear body assembly. *Proc. Natl. Acad. Sci. USA.* 112:E5237–E5245. https://doi.org/10.1073/pnas.1509317112

Brangwynne, C.P., C.R. Eckmann, D.S. Courson, A. Rybarska, C. Hoege, J. Gharakhani, F. Jülicher, and A.A. Hyman. 2009. Germline P granules are liquid droplets that localize by controlled dissolution/condensation. *Science.* 324:1729–1732. https://doi.org/10.1126/science.1172046

Elbaum-Garfinkle, S. 2019. Matter over mind: Liquid phase separation and neurodegeneration. *J. Biol. Chem.* 294:7160–7168. https://doi.org/10.1074/jbc.REV118.001188

Figley, M.D., G. Bieri, R.M. Kolaitis, J.P. Taylor, and A.D. Gitler. 2014. Profilin 1 associates with stress granules and ALS-linked mutations alter stress granule dynamics. *J. Neurosci.* 34:8083–8097. https://doi.org/10.1523/JNEUROSCI.0543-14.2014

Fros, J.J., N.E. Domeradzka, J. Baggen, C. Geertsema, J. Flipse, J.M. Vlak, and G.P. Pijlman. 2012. Chikungunya virus nsP3 blocks stress granule assembly by recruitment of G3BP into cytoplasmic foci. *J. Virol.* 86:10873–10879. https://doi.org/10.1128/JVI.01506-12

Frottin, F., F. Schueder, S. Tiwary, R. Gupta, R. Körner, T. Schlichthaerle, J. Cox, R. Jungmann, F.U. Hartl, and M.S. Hipp. 2019. The nucleolus functions as a phase-separated protein quality control compartment. *Science.* 365:342–347. https://doi.org/10.1126/science.aaw9157

Galganski, L., M.O. Urbanek, and W.J. Krzyzosiak. 2017. Nuclear speckles: molecular organization, biological function and role in disease. *Nucleic Acids Res.* 45:10350–10368. https://doi.org/10.1093/nar/gkx759

Guillén-Boixet, J., A. Kopach, A.S. Holehouse, S. Wittmann, M. Jahnel, R. Schlüßler, K. Kim, I.R.E.A. Trussina, J. Wang, D. Mateju, et al. 2020. RNA-Induced Conformational Switching and Clustering of G3BP Drive Stress Granule Assembly by Condensation. *Cell.* 181:346–361.e17. https://doi.org/10.1016/j.cell.2020.03.049

Harmon, T.S., A.S. Holehouse, M.K. Rosen, and R.V. Pappu. 2017. Intrinsically disordered linkers determine the interplay between phase separation and gelation in multivalent proteins. *eLife.* 6:e30294. https://doi.org/10.7554/eLife.30294

Jain, S., J.R. Wheeler, R.W. Walters, A. Agrawal, A. Barsic, and R. Parker. 2016. ATPase-Modulated Stress Granules Contain a Diverse Proteome and Substructure. *Cell.* 164:487–498. https://doi.org/10.1016/j.cell.2015.12.038

Kedersha, N., M.R. Cho, W. Li, P.W. Yacono, S. Chen, N. Gilks, D.E. Golan, and P. Anderson. 2000. Dynamic shuttling of TIA-1 accompanies the recruitment of mRNA to mammalian stress granules. *J. Cell Biol.* 151:1257–1268. https://doi.org/10.1083/jcb.151.6.1257

Kedersha, N., P. Ivanov, and P. Anderson. 2013. Stress granules and cell signaling: more than just a passing phase? *Trends Biochem. Sci.* 38:494–506. https://doi.org/10.1016/j.tibs.2013.07.004

Kedersha, N., M.D. Panas, C.A. Achorn, S. Lyons, S. Tisdale, T. Hickman, M. Thomas, J. Lieberman, G.M. McInerney, P. Ivanov, and P. Anderson. 2016. G3BP-Caprin1-USP10 complexes mediate stress granule condensation and associate with 40S subunits. *J. Cell Biol.* 212:845–860. https://doi.org/10.1083/jcb.201508028

Khong, A., T. Matheny, S. Jain, S.F. Mitchell, J.R. Wheeler, and R. Parker. 2017. The Stress Granule Transcriptome Reveals Principles of mRNA Accumulation in Stress Granules. *Mol. Cell.* 68:808–820.e5. https://doi.org/10.1016/j.molcel.2017.10.015

Lui, J., L.M. Castelli, M. Pizzinga, C.E. Simpson, N.P. Hoyle, K.L. Bailey, S.G. Campbell, and M.P. Ashe. 2014. Granules harboring translationally active mRNAs provide a platform for P-body formation following stress. *Cell Rep.* 9:944–954. https://doi.org/10.1016/j.celrep.2014.09.040

Mackenzie, I.R., A.M. Nicholson, M. Sarkar, J. Messing, M.D. Purice, C. Pottier, K. Annu, M. Baker, R.B. Perkerson, A. Kurti, et al. 2017. TIA1 Mutations in Amyotrophic Lateral Sclerosis and Frontotemporal Dementia Promote Phase Separation and Alter Stress Granule Dynamics. *Neuron.* 95:808–816.e9. https://doi.org/10.1016/j.neuron.2017.07.025

Markmiller, S., S. Soltanieh, K.L. Server, R. Mak, W. Jin, M.Y. Fang, E.C. Luo, F. Krach, D. Yang, A. Sen, et al. 2018. Context-Dependent and Disease-Specific Diversity in Protein Interactions within Stress Granules. *Cell.* 172:590–604.e13. https://doi.org/10.1016/j.cell.2017.12.032

Martin, A.N., and Y. Li. 2007. RNase MRP RNA and human genetic diseases. *Cell Res.* 17:219–226. https://doi.org/10.1038/sj.cr.7310120

Mathieu, C., R.V. Pappu, and J.P. Taylor. 2020. Beyond aggregation: Pathological phase transitions in neurodegenerative disease. *Science.* 370: 56–60. https://doi.org/10.1126/science.abb8032

Misteli, T. 2001. The concept of self-organization in cellular architecture. *J. Cell Biol.* 155:181–186. https://doi.org/10.1083/jcb.200108110

Misteli, T. 2008. Nuclear order out of chaos. *Nature.* 456:333–334. https://doi.org/10.1038/456333a

Mitrea, D.M., J.A. Cika, C.S. Guy, D. Ban, P.R. Banerjee, C.B. Stanley, A. Nourse, A.A. Deniz, and R.W. Kriwacki. 2016. Nucleophosmin integrates within the nucleolus via multi-modal interactions with proteins displaying R-rich linear motifs and rRNA. *eLife.* 5:e13571. https://doi.org/10.7554/eLife.13571

Mitrea, D.M., J.A. Cika, C.B. Stanley, A. Nourse, P.L. Onuchic, P.R. Banerjee, A.H. Phillips, C.G. Park, A.A. Deniz, and R.W. Kriwacki. 2018. Self-interaction of NPM1 modulates multiple mechanisms of liquid-liquid phase separation. *Nat. Commun.* 9:842. https://doi.org/10.1038/s41467-018-03255-3

Mollet, S., N. Cougot, A. Wilczynska, F. Dautry, M. Kress, E. Bertrand, and D. Weil. 2008. Translationally repressed mRNA transiently cycles through stress granules during stress. *Mol. Biol. Cell.* 19:4469–4479. https://doi.org/10.1091/mbc.e08-05-0499

Molliex, A., J. Temirov, J. Lee, M. Coughlin, A.P. Kanagaraj, H.J. Kim, T. Mittag, and J.P. Taylor. 2015. Phase separation by low complexity domains promotes stress granule assembly and drives pathological fibrillization. *Cell.* 163:123–133. https://doi.org/10.1016/j.cell.2015.09.015

Nedelsky, N.B., and J.P. Taylor. 2019. Bridging biophysics and neurology: aberrant phase transitions in neurodegenerative disease. *Nat. Rev. Neurol.* 15:272–286. https://doi.org/10.1038/s41582-019-0157-5

Neugebauer, K.M. 2017. Special focus on the Cajal Body. *RNA Biol.* 14:669–670. https://doi.org/10.1080/15476286.2017.1316928

Ojha, S., S. Malla, and S.M. Lyons. 2020. snoRNPs: Functions in Ribosome Biogenesis. *Biomolecules.* 10:783. https://doi.org/10.3390/biom10050783

Panas, M.D., T. Ahola, and G.M. McInerney. 2014. The C-terminal repeat domains of nsP3 from the Old World alphaviruses bind directly to G3BP. *J. Virol.* 88:5888–5893. https://doi.org/10.1128/JVI.00439-14

Ribbeck, K., and D. Görlich. 2002. The permeability barrier of nuclear pore complexes appears to operate via hydrophobic exclusion. *EMBO J.* 21: 2664–2671. https://doi.org/10.1093/emboj/21.11.2664

Sanders, D.W., N. Kedersha, D.S.W. Lee, A.R. Strom, V. Drake, J.A. Riback, D. Bracha, J.M. Eeftens, A. Iwanicki, A. Wang, et al. 2020. Competing Protein-RNA Interaction Networks Control Multiphase Intracellular Organization. *Cell.* 181:306–324.e28. https://doi.org/10.1016/j.cell.2020.03.050

Schisa, J.A. 2019. Germ Cell Responses to Stress: The Role of RNP Granules. *Front. Cell Dev. Biol.* 7:220. https://doi.org/10.3389/fcell.2019.00220

Tauber, D., G. Tauber, and R. Parker. 2020. Mechanisms and Regulation of RNA Condensation in RNP Granule Formation. *Trends Biochem. Sci.* 45: 764–778. https://doi.org/10.1016/j.tibs.2020.05.002

Van Treeck, B., D.S.W. Protter, T. Matheny, A. Khong, C.D. Link, and R. Parker. 2018. RNA self-assembly contributes to stress granule formation and defining the stress granule transcriptome. *Proc. Natl. Acad. Sci. USA.* 115:2734–2739. https://doi.org/10.1073/pnas.1800038115

Yang, P., C. Mathieu, R.M. Kolaitis, P. Zhang, J. Messing, U. Yurtsever, Z. Yang, J. Wu, Y. Li, Q. Pan, et al. 2020. G3BP1 Is a Tunable Switch that Triggers Phase Separation to Assemble Stress Granules. *Cell.* 181: 325–345.e28. https://doi.org/10.1016/j.cell.2020.03.046

Youn, J.Y., B.J.A. Dyakov, J. Zhang, J.D.R. Knight, R.M. Vernon, J.D. Forman-Kay, and A.C. Gingras. 2019. Properties of Stress Granule and P-Body Proteomes. *Mol. Cell.* 76:286–294. https://doi.org/10.1016/j.molcel.2019.09.014

Zhang, P., B. Fan, P. Yang, J. Temirov, J. Messing, H.J. Kim, and J.P. Taylor. 2019. Chronic optogenetic induction of stress granules is cytotoxic and reveals the evolution of ALS-FTD pathology. *eLife.* 8:e39578. https://doi.org/10.7554/eLife.39578

Supplemental material

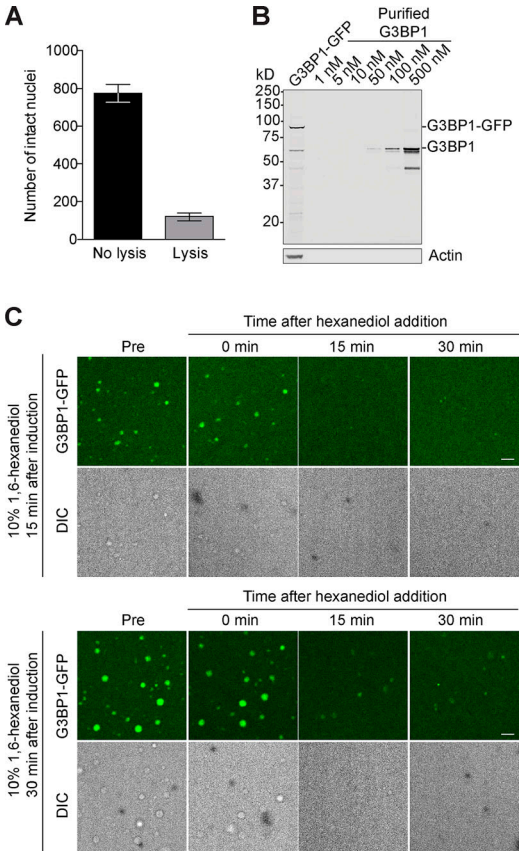

Figure S1. **Additional characterization of G3BP1 lysate granules. (A)** Cell pellets were resuspended in lysis buffer with or without 0.5% NP-40, and Hoechst was added. Quantification of Hoechst staining shows that a substantial portion of nuclei were lysed, and relatively few nuclei remain intact in the lysis buffer. Graph represents mean ± SD, n = 5 independent representative fields. **(B)** Western blot of U2OS or G3BP1-GFP U2OS lysates against purified G3BP1 standards. Cellular concentrations of G3BP1 were assessed by densitometry to be ~100 nM endogenous G3BP1 and 150 nM G3BP1-GFP in G3BP1-GFP U2OS lysate, for a total of 250 nM total G3BP1 in G3BP1-GFP U2OS cells. **(C)** Lysate granules were treated with 10% 1,6-hexanediol at 15 or 30 min following induction by increasing concentration of G3BP1 by 20 µM using purified G3BP1, leading to clearance of the lysate granules over time. Granules were visualized by imaging G3BP1-GFP or DIC. Scale bar, 5 µm.

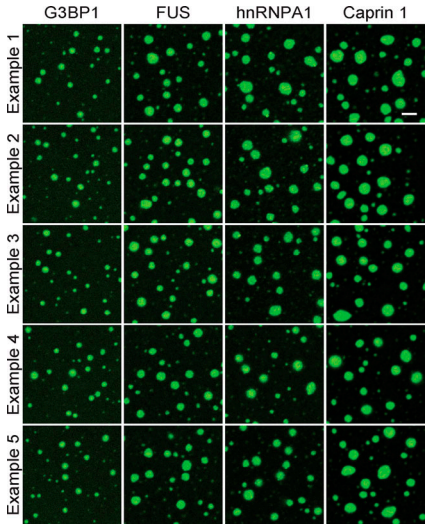

Figure S2. **A panel of representative images used for quantification of Fig. 2 C.** Scale bar, 5 µm.

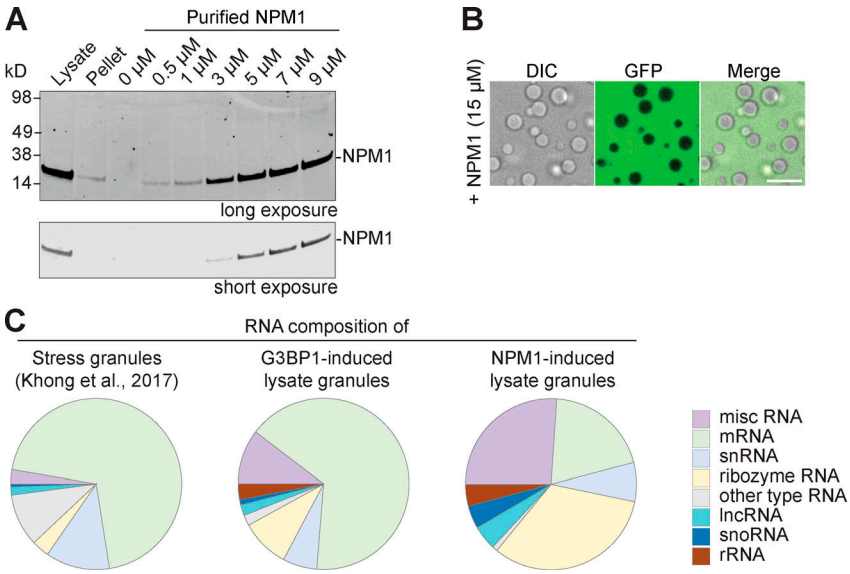

Figure S3. **Additional characterization of NPM1 lysate granules and RNA composition. (A)** Western blot of U2OS lysate (supernatant) and pellet run against a purified NPM1 standard. Concentrations were assessed by densitometry to be ~8.4 µM NPM1 in the cell (7.7 µM in soluble fraction and 0.7 µM in the pellet). **(B)** Addition of purified NPM1 protein (increasing concentration by 15 µM) to a cell lysate stably expressing GFP induces LLPS, but GFP does not localize to NPM1-induced lysate granules as visualized with DIC. Scale bar, 10 µm. **(C)** RNA composition of stress granules (Khong et al., 2017; left), G3BP1 lysate granules (center), and NPM1 lysate granules (right) analyzed by RNA-seq.

Video 1. **Formation, growth, and fusion of granules from G3BP1-GFP U2OS lysate induced with purified G3BP1.** Video shows a zoomed-out field of the granule shown in Fig. 1 F. Imaging was performed using time-lapse spinning-disk confocal microscopy of granules settled at the surface of the imaging chamber 5 min after induction of granules by increasing the concentration of G3BP1 by 20 µM using purified G3BP1. DIC and G3BP1-GFP images were captured every 0.083 min for 25 min total. Frames per second = 30.

Video 2. **Fusion of granules from G3BP1-GFP U2OS lysate induced with purified G3BP1.** The same granule is shown in Fig. 1 F; also a zoom-in of Video 1. Imaging was performed using time-lapse spinning-disk confocal microscopy of granules settled at the surface of the imaging chamber 5 min after induction of granules by increasing the concentration of G3BP1 by 20 µM using purified G3BP1. DIC and G3BP1-GFP images were captured every 0.083 min for 25 min total. Frames per second = 30.

Video 3. **FRAP of G3BP1-GFP from lysate granules induced at various G3BP1 concentrations.** Video corresponds to the FRAP curves shown in Fig. 1 G. Imaging was performed using time-lapse spinning-disk confocal microscopy of granules settled at the surface of the imaging chamber 30 min after induction of granules with purified G3BP1. Arrows indicate lysate granules on which FRAP was performed. Images were captured every 0.2 s for 35 s total. Photobleaching with 488-nm laser occurred 2 s into capture. Frames per second = 15.

Video 4. **FRAP of G3BP1-GFP and GFP-ATXN2L within cellular stress granules (SGs).** Video corresponds to stills and FRAP curves shown in Fig. 2, F and G. Stable G3BP1-GFP or KI GFP-ATXN2L U2OS cells were exposed to 500 µM sodium arsenite for 30 min. Imaging was performed using time-lapse spinning-disk confocal microscopy of cells adhering to the surface of the imaging chamber. Arrows indicate stress granules on which FRAP was performed. Images were captured every 0.1 s for 35 s total. Photobleaching with 488-nm laser occurred 2 s into capture. Frames per second = 30.

Video 5. **FRAP of G3BP1-GFP and GFP-ATXN2L within G3BP1-induced lysate granules.** Video corresponds to stills and FRAP curve shown in Fig. 2, H and I. Lysates from stable G3BP1-GFP or KI GFP-ATXN2L U2OS cells were induced by increasing the concentration of G3BP1 by 20 µM using purified G3BP1. Imaging was performed using time-lapse spinning-disk confocal microscopy of granules settled at the surface of the imaging chamber. Arrows indicate lysate granules on which FRAP was performed. Images were captured every 0.2 s for 35 s total. Photobleaching with 488-nm laser occurred 2 s into capture. Frames per second = 15.

Video 6. **FRAP of transfected GFP-NPM1 in the nucleolus and NPM1-induced lysate granules.** Video corresponds to stills and FRAP curves shown in Fig. 4, B and C. U2OS cells were transiently transfected with GFP-NPM1. Intact transfected cells were imaged to monitor mobility of GFP-NPM1 in the nucleolus. Lysates prepared from transfected cells were induced by increasing the concentration of NPM1 by 15 µM using purified NPM1. Imaging was performed using time-lapse spinning-disk confocal microscopy of granules settled at the surface or cells adhering to the surface of the imaging chamber. Arrows indicate nucleolus and NPM1-induced lysate granule on which FRAP was performed. Images were captured every 0.2 s for 60 s total. Photobleaching with 488-nm laser occurred 2 s into capture. Frames per second = 30.

Provided online are five Excel tables. Table S1 shows protein composition of lysate granules formed by increasing the G3BP1 concentration of U2OS cell lysate from one 10-cm plate by 20 µM. Table S2 shows the RNA composition of G3BP1-induced lysate granules and stress granules (Khong et al., 2017) in fragments per kilobase of transcript per million mapped reads (FPKM) and TPM. Table S3 shows percent composition of RNA by subtype of lysate granules and stress granules (Khong et al., 2017), percent composition of RNA by subtype of granules formed in G3BP1 lysate granules versus RNA found in stress granules (Khong et al., 2017; tab 1), and percent composition of RNA by subtype in NPM1 lysate granules (tab 2). Table S4 shows protein composition of lysate granules formed by increasing the NPM1 concentration of U2OS cell lysate from one 10-cm plate by 15 µM. Table S5 shows RNA composition of NPM1-induced lysate granules in fragments per kilobase of transcript per million mapped reads (FPKM) and TPM.